

## THE DENSITY FIELD OF THE 10K zCOSMOS GALAXIES<sup>1</sup>

K. KOVAČ<sup>2</sup>, S. J. LILLY<sup>2</sup>, O. CUCCIATI<sup>3</sup>, C. PORCIANI<sup>2,18</sup>, A. IOVINO<sup>3</sup>, G. ZAMORANI<sup>4</sup>, P. OESCH<sup>2</sup>, M. BOLZONELLA<sup>4</sup>, C. KNOBEL<sup>2</sup>, A. FINOGENOV<sup>5</sup>, Y. PENG<sup>2</sup>, C. M. CAROLLO<sup>2</sup>, L. POZZETTI<sup>4</sup>, K. CAPUTI<sup>2</sup>, J. D. SILVERMAN<sup>2</sup>, L. TASCA<sup>6</sup>, M. SCODEGGIO<sup>7</sup>, D. VERGANI<sup>7</sup>, E. ZUCCA<sup>4</sup>, T. CONTINI<sup>8</sup>, J.-P. KNEIB<sup>6</sup>, O. LE FÈVRE<sup>6</sup>, V. MAINIERI<sup>9</sup>, A. RENZINI<sup>10</sup>, N. Z. SCOVILLE<sup>11</sup>, P. CAPAK<sup>12,11</sup>, S. BARDELLI<sup>4</sup>, A. BONGIORNO<sup>5</sup>, G. COPPA<sup>4</sup>, S. DE LA TORRE<sup>6</sup>, L. DE RAVEL<sup>6</sup>, P. FRANZETTI<sup>7</sup>, B. GARILLI<sup>7</sup>, L. GUZZO<sup>3</sup>, P. KAMPCZYK<sup>2</sup>, F. LAMAREILLE<sup>8</sup>, J.-F. LE BORGNE<sup>8</sup>, V. LE BRUN<sup>6</sup>, C. MAIER<sup>2</sup>, M. MIGNOLI<sup>4</sup>, R. PELLO<sup>6</sup>, E. PEREZ MONTERO<sup>6</sup>, E. RICCIARDELLI<sup>10</sup>, M. TANAKA<sup>9</sup>, L. TRESSE<sup>6</sup>, U. ABBAS<sup>6,19</sup>, D. BOTTINI<sup>7</sup>, A. CAPPI<sup>4</sup>, P. CASSATA<sup>6</sup>, A. CIMATTI<sup>13</sup>, M. FUMANA<sup>7</sup>, D. MACCAGNI<sup>7</sup>, C. MARINONI<sup>14</sup>, H. J. MCCRACKEN<sup>15</sup>, P. MEMEO<sup>7</sup>, B. MENEUX<sup>5,16</sup>, R. SCARAMELLA<sup>17</sup>, A. M. KOEKEMOER<sup>20</sup>

*Draft version June 6, 2018*

### ABSTRACT

We use the current sample of  $\sim 10,000$  zCOSMOS spectra of sources selected with  $I_{AB} < 22.5$  to define the density field out to  $z \sim 1$ , with much greater resolution in the radial dimension than has been possible with either photometric redshifts or weak lensing. We apply new algorithms that we have developed (ZADE) to incorporate objects not yet observed spectroscopically by modifying their photometric redshift probability distributions using the spectroscopic redshifts of nearby galaxies. This strategy allows us to probe a broader range of galaxy environments and reduce the Poisson noise in the density field. The reconstructed overdensity field of the 10k zCOSMOS galaxies consists of cluster-like patterns surrounded by void-like regions, extending up to  $z \sim 1$ . Some of these structures are very large, spanning the  $\sim 50 \text{ h}^{-1} \text{ Mpc}$  transverse direction of the COSMOS field and extending up to  $\Delta z \sim 0.05$  in redshift. We present the three dimensional overdensity maps and compare the reconstructed overdensity field to the independently identified virialised groups of galaxies and clusters detected in the visible and in X-rays. The distribution of the overdense structures is in general well traced by these virialised structures. A comparison of the large scale structures in the zCOSMOS data and in the mock catalogues reveals an excellent agreement between the fractions of the volume enclosed in structures of all sizes above a given overdensity between the data and the mocks in  $0.2 < z < 1$ .

*Subject headings:* galaxies: high-redshift — (cosmology:) large-scale structure of universe — surveys

### 1. INTRODUCTION

Although on scales larger than  $\sim 100 \text{ h}^{-1} \text{ Mpc}$  the universe is homogeneous and isotropic, on smaller scales structures in the universe are organised hierarchically. The full view of the cosmic structure was revealed for the first time in the first CfA-II slice (de Lapparent et al. 1986), with galaxies distributed in bubble like structures surrounding empty regions. Later surveys, particularly the Sloan Digital Sky Survey (SDSS, York et al. 2000) and the two-degree Field Galaxy Redshift Survey (2dFGRS, Colless et al. 2001), have confirmed the highly complex hierarchical picture of the universe at  $z \sim 0$ . Our universe exhibits a range of cellular structures, the cosmic-web (Bond et al. 1996), where galaxies define the structures which form patterns of dense compact clusters, elongated filaments and sheet-like walls outlining large and almost empty voids. While the network of filaments and clumps sitting in the intersection of filaments dominate the visual impression of the cosmic web, most of the volume is in the underdense regions (voids).

The picture emerging from the surveys of the higher redshift universe is limited by small fields and cosmic variance, but the richness and complexity of the cosmic web appears (at least visually) to match that of the local universe out to

<sup>1</sup> Based on observations obtained at the European Southern Observatory (ESO) Very Large Telescope (VLT), Paranal, Chile, as part of the Large Program 175.A-0839 (the zCOSMOS Spectroscopic Redshift Survey)

<sup>2</sup> Institute of Astronomy, ETH Zurich, 8093 Zurich, Switzerland

<sup>3</sup> INAF Osservatorio Astronomico di Brera, Milan, Italy

<sup>4</sup> INAF Osservatorio Astronomico di Bologna, via Ranzani 1, I-40127, Bologna, Italy

<sup>5</sup> Max-Planck-Institut für extraterrestrische Physik, D-84571 Garching, Germany

<sup>6</sup> Laboratoire d'Astrophysique de Marseille, Marseille, France

<sup>7</sup> INAF - IASF Milano, Milan, Italy

<sup>8</sup> Laboratoire d'Astrophysique de l'Observatoire Midi- Pyrénées, Toulouse, France

<sup>9</sup> European Southern Observatory, Karl-Schwarzschild- Strasse 2, Garching, D-85748, Germany

<sup>10</sup> Dipartimento di Astronomia, Università di Padova, Padova, Italy

<sup>11</sup> California Institute of Technology, MS 105-24, Pasadena, CA 91125, USA

<sup>12</sup> Spitzer Science Center, 314-6 Caltech, Pasadena, CA 91125, USA

<sup>13</sup> Dipartimento di Astronomia, Università di Bologna, via Ranzani 1, I-40127, Bologna, Italy

<sup>14</sup> Centre de Physique Théorique, Marseille, France

<sup>15</sup> Institut d'Astrophysique de Paris, UMR 7095 CNRS, Université Pierre et Marie Curie, 98 bis Boulevard Arago, F-75014 Paris, France.

<sup>16</sup> Universitäts-Sternwarte, Scheinerstrasse 1, D-81679 Muenchen, Germany

<sup>17</sup> INAF, Osservatorio di Roma, Monteporzio Catone (RM), Italy

<sup>18</sup> Argelander Institut für Astronomie, Auf dem Hügel 71, D-53121 Bonn, Germany

<sup>19</sup> ELSA Marie Curie Postdoctoral Fellow, INAF - Osservatorio Astronomico di Torino, 10025 Pino Torinese, Italy

<sup>20</sup> Space Telescope Science Institute, 3700 San Martin Drive, Baltimore, MD 21218, USA

$z \sim 1.5$  (e.g. Scoville et al. 2007b; Marinoni et al. 2008). As redshift increases, the peak in the probability distribution function of the galaxy overdensity field shifts towards lower overdensity values, and the fraction of the volume in the underdense regions decreases (Marinoni et al. 2008).

The galaxy distribution is believed to be a (biased) tracer of the underlying smooth and continuous matter density field. It has been shown by numerical simulations and by analytical work that the observed large scale structure (LSS) pattern is a natural manifestation of the gravitational structure formation process through the amplification of density fluctuations and their subsequent collapse. The presence of the cosmic web can be explained with the tendency of the matter concentrations to contract and collapse gravitationally in an anisotropic manner (Bond et al. 1996; van de Weygaert & Bertschinger 1996).

One of the main characteristics of the cosmic-web is its hierarchical nature. The LSS structures cover a broad range in (over)density values, physical scales and geometrical shapes. The reconstruction of the density field from an observed galaxy sample should ideally preserve all these features. However, the samples of the galaxies are incomplete, particularly at high redshifts, and the sampling is often irregular. Different galaxy populations evolve with redshift in different ways, and they may trace the underlying mass distribution in different ways at different redshifts. On top of this, one has to add an uncertainty in the measured redshifts, magnitudes and other galaxy properties. All of these points make the reconstruction of the density field in the Universe non trivial.

The reconstruction of a continuous, presumably smooth field from a set of measured discrete data points usually involves the interpolation and smoothing of the data with some filtering function into a continuous map. Unlike the velocity or temperature fields for which we sample the field values in the observed points, for the density field reconstruction there are no field samples available. The measured data points (galaxies) are used to define the density field itself. A common feature of all the available approaches to reconstruct the density field is that the results of the reconstructed density field depend on the method used to carry out the reconstruction. Usually a particular scientific application guides the choice of the method to reconstruct the density field, and we briefly review these here.

### 1.1. *Applications of the density field*

#### 1.1.1. *Extraction of the components of the cosmic web*

An immediate application of the reconstructed density field is the extraction of the four components of the cosmic web (clumps, filaments, sheets and voids). While the human eye can easily distinguish between these shapes, there does not exist an ideal algorithm yet to extract these features in an algorithmically well-defined way. A lot of progress has been made recently, by applying a geometrical classification directly to the density field, such as the multi-scale analysis of the Hessian matrix of the density field (Aragón-Calvo et al. 2007) or the skeleton analysis of the density field (Novikov et al. 2006; Sousbie et al. 2008). Alternatively, a classification of the cosmic web can be done using either a linear (Lee & Lee 2008) or non-linear (Hahn et al. 2007a,b; Forero-Romero et al. 2008) gravitational potential. Some of these methods have been applied so far only on numerical simulations and result in the classification of the dark matter structures. The reconstruction of the density field from observed galaxy data is based on a very much smaller number of objects, and therefore it lacks the spatial resolution of the simulations. However, probably the most difficult task to tackle is that the observations provide information on the position of galaxies in redshift space, while for the proper reconstruction of the cosmic web galaxy positions need to be measured in real space (Lee & Lee 2008; Lee & Li 2008). This is not of course a problem in simulations.

#### 1.1.2. *Correlation between galaxies and environment in which they reside*

Several correlations between galaxy properties and the environments in which they reside are observed in the local Universe. In this context, the environment of a galaxy is given by the number density (or overdensity) of the neighbouring galaxies. It has been known for many years that elliptical and lenticular galaxies reside in more dense environments than spiral galaxies (e.g. Dressler 1980). Red, older, less star forming galaxies live in more dense regions than blue, younger galaxies with high star formation rates (e.g. Kauffmann et al. 2004; Blanton et al. 2006). These trends are observed in environments ranging from clusters to voids.

Are the early conditions of galaxy formation (the so-called nature scenario) or the environment in which they subsequently reside (the so-called nurture scenario), or both of these, responsible for the observed dependences of galaxy properties on environment? An obvious way to tackle this question is to go to higher redshifts and to establish at which redshift the relations in question are in place. Not long ago, high redshift observations were limited to the most dense structures (i.e. clusters) or targeted to detect a specific galaxy population (e.g. Lyman break galaxies or Ly $\alpha$  emitters). Large and deep redshift surveys are the best probes of the (over-)density field delineated by galaxies at all redshifts. The recent spectroscopic high redshift surveys, the DEEP2 Galaxy Redshift Survey (Davis et al. 2003) and the VVDS (Le Fèvre et al. 2005) and now zCOSMOS (Lilly et al. 2007, 2008 in prep), sample the broad range of galaxy population and allow the continuous reconstruction of galaxy environments. Most of the galaxy property-environment relations observed at  $z \sim 0$  seems to be at place already at  $z \sim 1$  (e.g. Cucciati et al. 2006; Cooper et al. 2007).

Even in the local Universe, there is an ongoing debate on whether the observed galaxy-environment relations depend on the particular scale at which the environment has been measured. This would potentially give a clue to their origin. Kauffmann et al. (2004) and Blanton et al. (2006) both find that only the environment measured on the small scales (of  $1 h^{-1} \text{Mpc}$ ) appears to affect the star formation histories of galaxies. In the context of the CDM scenario, this scale corresponds to the scale of the individual dark matter halo in which galaxy resides, whereas the larger scale would

probe more the location in the cosmic web.

In the current state of the art of the high redshift surveys, it is very challenging to reconstruct environments on such a small scale. Galaxies targeted for the observations at higher redshifts are generally more luminous, and their mean inter-galaxy separations are thus larger. Furthermore, only a fraction of galaxies is targeted for the observations, and this fraction may be substantially smaller than locally.

### 1.1.3. Galaxy density field as biased tracer of the matter density field

In the current cosmological picture it is almost a paradigm that galaxies are a biased tracer of the underlying matter distribution. The biasing factor can be a non-trivial function of the scale, of the redshift and of the type of galaxies used to reconstruct the density field. Using a statistical approach, one of the ways to infer the biasing function is from a comparison of the probability distribution functions (PDF) of the galaxy and matter overdensities (Sigad et al. 2000; Marinoni et al. 2005). While the first is based on observations, the PDF of the matter comes from theory and is dependent on the assumed cosmological parameters. In the case of the three dimensional overdensities reconstructed with a top-hat filter, the PDF of the matter is well described by the log-normal distribution (Coles & Jones 1991).

### 1.2. Goals of this study

The main goal of this paper is to reconstruct the galaxy overdensity field in the zCOSMOS region. We reconstruct the overdensity field using the first  $\sim 10,000$  spectra of galaxies from the zCOSMOS survey, up to redshift  $z \sim 1$  (Lilly et al. 2008 in prep), the so-called 10k sample. High sampling rate and measurements of redshifts with a precision of about  $100 \text{ km s}^{-1}$  enable us to delineate the environments of galaxies from the 100 kpc scale of galaxy groups – the scale of environment expected to dominate the various galaxy evolutionary processes – up to the 100 Mpc scales of the cosmic web. It is one of the major scientific drivers of the zCOSMOS survey to study the role of environment on galaxy evolution up to high redshifts. We therefore pay particular attention to reconstruct the density field on scales that are as small as possible. With this aim, a new method (ZADE, Kovač et al. b, in prep) has been developed to reconstruct the density field using both galaxies with spectroscopic redshifts, and those with only photometric redshifts. The photometric probability distribution functions are modified depending on the proximity of galaxies with high quality spectroscopic redshifts. We utilise this method to reconstruct the overdensity field at the positions of the 10k zCOSMOS galaxies and in any random point in the zCOSMOS volume. The reconstruction has been carried out in a number of ways so as to facilitate a wide range of scientific explorations as discussed above. We present the three dimensional overdensity maps, and compare the LSS structures in the overdensity field to the independently estimated virialised structures in the volume of the zCOSMOS survey. Extensive use is made of COSMOS mock catalogues (Kitzbichler & White 2007) to estimate the errors on the reconstructed overdensity field and to compare the zCOSMOS overdensity field to those obtained from the mock catalogues. Throughout this paper, we assume a flat cosmology described with  $\Omega_{m,0} = 0.25$  and  $H_0 = 70 \text{ km s}^{-1}$ . However, we express the results related to the overdensity field using  $h$ ,  $H_0 = 100h$ , while stellar masses and absolute magnitudes of galaxies are quoted with an explicitly incorporated  $H_0 = 70 \text{ km s}^{-1}$ .

In follow-up papers, we study the dependence of star formation properties (Cucciati et al. in prep) and morphology (Tasca et al. in prep) on the environments of the 10k zCOSMOS galaxies presented in this paper. The environmental dependence of the luminosity and mass functions is discussed in Zucca et al. (in prep) and Bolzonella et al. (in prep), respectively. The biasing function between the zCOSMOS and matter overdensity fields is presented in Kovač et al. (a, in prep). Other studies cover environmental dependence of specific galaxy populations, such as IR galaxies (Caputi et al. 2008), AGN (Silverman et al. submitted) or post-starburst galaxies (Vergani et al. in prep).

## 2. (GALAXY) DENSITY FIELD RECONSTRUCTION

A number of methods exist to evaluate the density field, often developed for numerical simulations, e.g. grid based methods, smooth particle hydrodynamics (SPH) like methods, Voronoi and Delaunay tessellation field estimators (VTFE and DTFE). Here, we concentrate on the problem of reconstruction of the density field from the observational data sample of galaxies.

In practice, reconstruction of the galaxy density field (or galaxy environments) reduces to the (weighted) count of objects within some aperture around a set of positions where the density field is to be evaluated. In the general case, the density at an observationally defined position  $\mathbf{r} = \mathbf{r}(\alpha, \delta, z)$  can be estimated as

$$\rho(\mathbf{r}) = \sum_i \frac{m_i W(|\mathbf{r} - \mathbf{r}_i|; R)}{\phi(\mathbf{r}_i)}. \quad (1)$$

The above equation gives the value of a mean density at a position  $\mathbf{r}$  in the redshift space (averaged over the aperture in which the density field is measured), with  $W$  a spatial window function,  $m_i$  a weight based on the astrophysical properties for each galaxy and  $\phi$  a function correcting for various observational issues. The difference  $|\mathbf{r} - \mathbf{r}_i|$  refers to any arbitrarily defined distance between observationally defined points.

The following points should be noted.

- The form of equation 1 which we use to define the density at a point is similar to the density estimate in the SPH simulations (e.g. Hernquist & Katz 1989), with the exception of the selection function  $\phi$ . The density can be evaluated at a position of a galaxy (the so-called scatter approach, e.g. Hernquist & Katz 1989), or at any

chosen point in space (the so-called gather approach, e.g. Hernquist & Katz 1989). The points can be of course chosen such that they form a regularly spaced grid.

- The summation in equation 1 goes over those galaxies in the sample that have been chosen to define the density field, which we refer to as *tracer* galaxies. These tracer galaxies might be all galaxies detected in the survey (which is commonly flux limited) or only a subsample of those satisfying some selection criteria, e.g. a criterion that is as much as possible independent of redshift, so as to form a “volume limited sample”.
- The function  $W(|\mathbf{r} - \mathbf{r}_i|; R)$  is the kernel used to weight the tracer galaxies, which is a spatial smoothing function (e.g. a top-hat or a Gaussian function) and  $R$  is the smoothing length. The  $W$  function is typically chosen such that it weights tracer galaxies depending on their distance  $|\mathbf{r} - \mathbf{r}_i|$  from the position where the density is being reconstructed. The distance between two points can be defined in various ways. In most of the applications the smoothing function  $W$  shows some symmetry with respect to the reconstruction point. Commonly, it is of fixed shape and normalised to unity, i.e.  $\int W dV = 1$ .
- The smoothing length  $R$  defines the aperture within which the environment is measured. To obtain a well defined value at every point, the field needs to be filtered over a large aperture, such that the shot-noise effects are suppressed. However, all properties of the density field on scales smaller than the smoothing filter  $R$  will be smoothed away. The smoothing length  $R$  in a given reconstruction procedure can be defined to be of fixed or adaptive size. The fixed scale is then the same at every point and should be chosen such that there are enough tracer galaxies within the smoothing kernel to be able to reliably reconstruct the density at a given point. Unfortunately, in order to keep the number of galaxies in low density regions reasonably large to obtain statistically meaningful results, the smoothing length  $R$  is then required to be rather large. The statistical fluctuations of the measured density will depend on the number of tracer galaxies within the smoothing aperture, i.e. on the density and will be statistically more accurate in the regions with higher density. On the other hand, the adaptive scale varies over the volume in which the density field is being reconstructed. It is given by the density of the neighbouring tracer galaxies, typically defined by the distance from the point of the density reconstruction (which can be a galaxy or any point in space) to the fixed  $N$ th nearest neighbour. The use of an adaptive scale leads to a larger dynamical range and higher spatial resolution (in the dense regions) with respect to the fixed scale and the purely Poisson noise can also be made constant for a given population of tracer galaxies.
- $m_i$  is the astrophysical weight (“mass”) of the tracer galaxy. In the reconstruction of galaxy density fields it usually has a value of unity for each tracer galaxies, producing a “number-density”. However,  $m_i$  can be any measured property of the tracer galaxies (e.g. stellar mass). In the ideal case, it would probably be the total mass of a tracer galaxy. The resulting “mass” weighted density is supposed to be related to the underlying matter density via the bias  $b$  factor. However, the bias can be a nonlinear and stochastic function, depending on the scale, redshift and type of the tracer galaxies.
- The reconstructed density field is supposed to be the density field based on the total population of chosen tracer galaxies in the observed volume. The function  $\phi$  may be introduced to correct for the fact that in reality only a fraction of the full population of tracer galaxies is at our disposal when reconstructing the density field. The function  $\phi$  should account for the observational restrictions such as the non-uniform sampling over the observed area, a radial selection function or the redshift success rate of the observed sources in the spectroscopic surveys. All of these constraints may depend on the intrinsic properties of galaxies (e.g. the luminosity or the morphological type) and as a result it may be very challenging to model all possible dependences into the  $\phi$  function.

Unavoidably, the properties of the reconstructed density field will depend on the adopted method. The choice of a particular reconstruction method, given by the exact functional forms of  $W(|\mathbf{r} - \mathbf{r}_i|; R)$ ,  $\phi(\mathbf{r}_i)$  and  $m_i$ , and the choice of the tracer galaxies, is guided primarily by the scientific goals, but it will always contain some level of user-specified arbitrariness. In particular, one has to optimise between the scale at which the environment is measured and the error of the environment reconstructed on that scale, arising because we are using discrete tracers. While it may be desirable to measure environments on a very small scale, the statistical errors for the smallest scales are also the largest (e.g. Blanton et al. 2003, see also our results on the mock catalogues in Section 4). For some interpretations of the scientific results it may be desirable to use a fixed scale to define the environment, because the adaptive scales are smaller in the denser regions and larger in empty regions. However, the adaptive scales prove to be superior over the fixed scales in preserving the complex morphology of the density field (e.g. Park et al. 2007).

One limitation of the outlined scheme is its lack of sensitivity to the geometry of the mass distribution: the used kernels are commonly of fixed shape and isotropic. Even smoothing with the adaptive scale will smear out the smallest structures, particularly the ones of anisotropic shapes (e.g. Romano-Díaz & van de Weygaert 2007). Shapiro et al. (1996) and Owen et al. (1998) introduced in simulations an elliptical kernel with axis ratio dependent on the geometrical distribution of particles.

The VTFE and DTFE are other methods to reconstruct the continuous density fields (Bernardeau & van de Weygaert 1996; Schaap & van de Weygaert 2000; Schaap 2007). Both VTFE and DTFE

are fully adaptive and volume covering methods based on the Voronoi and Delaunay tessellation of the point sample, respectively, which divide space into a space-filling network of polyhedral cells (Voronoi tessellation, Dirichlet 1850; Voronoi 1908) or mutually disjoint tetrahedral cells in three dimensions (Delaunay tessellation, Delone 1934) according to the local density and geometry of the sampling points. Therefore the VTFE and DTFE methods have the advantage over the methods which use kernels of fixed size to better recover the anisotropic structures in density fields, such as filaments and walls.

However, direct applications of the VTFE or DTFE to reconstruct the density field in the current  $z \sim 1$  and higher redshift surveys also have some drawbacks. First, the spectroscopic surveys at these redshifts have usually a small angular size on the sky (1-2 deg<sup>2</sup>), and with the current number density of the tracer galaxies the volumes of the Voronoi and Delaunay cells will be greatly affected at the edges. Cooper et al. (2005) used the Voronoi tessellation to estimate the local density of galaxies in the DEEP2-like mock catalogues. They conclude that more than 45% of the sample galaxies are affected by the edges when using the Voronoi tessellation to reconstruct densities around galaxies, compared with  $\sim 15\%$  when using a cylindrical kernel with  $R = 1 \text{ h}^{-1}\text{Mpc}$ . Second, in  $z \sim 1$  spectroscopic surveys the fraction of galaxies with a high quality spectrum, which leads to a reliable measure of a redshift used to delineate the density field, often is not greater than  $\sim 50\%$ . It has not been investigated which effects this sampling fraction will have on an asymmetric density estimator such as DTFE. Moreover, it is not clear how to deal with probabilistic objects in the VTFE or DTFE (see van Breukelen et al. 2006, who use a Monte Carlo approach to sample the photometric redshift probability function of galaxies in the Voronoi tessellation method). The DTFE patterns also contain some artefacts, the most prominent one being the triangular imprint of the smoothing kernel (Schaap 2007; Romano-Díaz & van de Weygaert 2007).

For some scientific applications, such as biasing, the density field needs to be reconstructed on a fixed scale. In a flux limited survey, the mean separation between galaxies will increase with the redshift for a given smoothing scale and increase the shot noise. Even a given population of galaxies will be characterised by some average inter-galaxy separation, and therefore with any given galaxy population the density field on scales smaller than this separation will be dominated by the shot noise. For fixed apertures, the Wiener filtering technique can be used to deconvolve the noise from the reconstructed density field (e.g. Lahav et al. 1994; Hoffman 1994; Zaroubi et al. 1995). This technique is based on the minimum variance reconstruction of the density field, which requires the noise model and power spectrum of the density field to be known a priori.

It is common to express the resulting measurement of density as a dimensionless density contrast  $\delta(\mathbf{r})$  (which we interchangeably refer to also as “overdensity”) defined as

$$\delta(\mathbf{r}) = \frac{\rho(\mathbf{r}) - \rho_m(z)}{\rho_m(z)}, \quad (2)$$

where  $\rho_m(z)$  is the mean density at a given redshift. In most of the applications  $\rho_m(z)$  is evaluated as a volume average, but it can be estimated also as an average over galaxies (e.g. Cooper et al. 2006). Although we generally refer to  $\delta$  also as “overdensity”, we will characterise regions with  $\delta > 0$  as being overdense, and regions with  $\delta < 0$  as being underdense.

### 3. ZADE METHODOLOGY

The photometric redshift technique enables us to obtain redshifts of large number of galaxies in relatively modest amount of observing time with respect to spectroscopic surveys. The obtained photometric redshifts can be used for a variety of applications, such as luminosity and mass functions. Clearly, spectroscopic redshifts offer a major improvement over even a high quality photometric redshifts. For instance, Cooper et al. (2005) find that for the density field reconstruction, if only the photometric redshifts are used, even with uncertainties as small as  $0.02(1+z)$ , the reconstructed environment in the line-of-sight direction is smeared out on small scales. Only for uncertainties of photometric redshifts smaller than 0.005 and when measuring densities in projection, photometric redshift surveys can become comparable to spectroscopic surveys in terms of environment reconstruction (Cooper et al. 2005). Including a properly devised background correction the projected density estimator based on photometric redshifts becomes substantially unbiased, even though with a large scatter. This background corrected estimator is robust for projected densities larger than 10 galaxies per  $(\text{h}^{-1}\text{Mpc})^2$  (Guzzo et al. 2007). However, the spectroscopic surveys with redshift uncertainties smaller than the velocity dispersion of the small group (i.e. below 200-250 km s<sup>-1</sup>) are the preferred source of data with redshift of sufficient precision to reconstruct the *small-scale environments* of galaxies.

To reconstruct the density field on the given scale and with acceptable error one needs to balance between two requirements: precise spectroscopic redshifts to accurately trace the overdense and underdense regions, but as large number of objects as possible to lower the noise and enable reconstruction of the density on the smaller scales.

We have developed a new algorithm (ZADE, Kovač et al. b, in prep) which brings together the accuracy of spectroscopic redshifts with the number statistics of the photometric redshifts, in order to broaden the scale of the reliable reconstructed environments. Motivated by the literature results of the importance of the scales at which the density is measured, our main effort has been made to reliably reconstruct the small scale environments. The algorithm modifies the individual redshift probability distributions  $P(z)$  that are output by a photometric redshift code (e.g. ZEBRA) based on the spectroscopic redshifts of galaxies located nearby on the sky.

It is well known that galaxies are highly correlated on scales up to  $10 \text{ h}^{-1}\text{Mpc}$ . Therefore, a galaxy that has only a photometric redshift probability function  $P(z)$ , is much more likely to lie at some redshifts than at others, depending on the accurately determined spectroscopic redshifts of other galaxies that lie near to the same line of sight.

As described in more detail in Kovač et al. (b, in prep), the ZADE algorithm modifies the initial  $P(z)$  that is output of the photometric redshift programme, by counting the number of objects with spectroscopic redshift within some radius ( $R_{ZADE}$ ) as a function of  $z$  along the line of sight, to yield a modified probability  $P_{ZADE}(z)$ :

$$P_{ZADE}(z) = \frac{N(\leq R_{ZADE}, z) \times P(z)}{\int N(\leq R_{ZADE}, z) \times P(z) dz}. \quad (3)$$

In Figure 1 we show two examples of the ZADE approach to modify the initial  $P(z)$ , obtained using the ZEBRA code (Feldmann et al. 2006). For the computing purposes, we discretise the ZADE-modified  $P(z)$  of every galaxy in  $\Delta z = 0.002$  (this does not match the ZEBRA precision). At the current state of the uncertainty in the photometric redshifts, there are typically a few structures within the  $P(z)$  along a given line of sight (effectively distribution of galaxies within  $R_{ZADE}$ ), so the ZADE approach is only statistical.

ZADE has been extensively tested on mock catalogues. We tested our method using five different  $R_{ZADE}$  values: 1, 2.5, 5, 7.5 and 10  $h^{-1}$ Mpc, even though in Figure 1 we show results only for three of them (1, 5 and 10  $h^{-1}$ Mpc). The value  $R_{ZADE} = 5 h^{-1}$ Mpc is chosen as an optimal ZADE radius to modify the photometric probability functions in order to reconstruct the density field without any systematics.

In Kovač et al. (b, in prep) we conclude that the use of the combination of objects with the spectroscopic and ZADE-modified photometric redshifts reconstructs the overdensity field at a given scale with smaller errors than the traditional approach of using only the spectroscopic sample of objects weighted with some  $\phi(\mathbf{r}_i)$  function in equation 1 (which in our tests accounts for a non uniform  $RA - DEC$  sampling). Therefore, this enables us to use smaller smoothing scales in the reconstruction process, and thereby broadens the dynamical range of the reconstructed environments.

For every density reconstruction within the zCOSMOS survey we use this combination of galaxies with spectroscopic and ZADE modified photometric redshifts. The summation in equation 1 is therefore over all galaxies of a given population in the survey volume (and not only over a fraction of galaxies with reliable spectroscopic redshifts) equivalent to setting  $\phi(\mathbf{r}_i) = 1$  for every tracer galaxy. This is one of the major advantages of using galaxies with both spectroscopic and photometric redshifts, because in practice it is impossible to model the  $\phi(\mathbf{r}_i)$  function in such a way to take into account all the complex selection effects of most spectroscopic surveys. In equation 1, galaxies with only photometric redshift will be counted with their ZADE-modified  $P_{ZADE}(z)$  according to a smoothing filter  $W$ .

#### 4. RECONSTRUCTING THE DENSITY FIELD WITHIN THE zCOSMOS VOLUME

##### 4.1. zCOSMOS survey

zCOSMOS (Lilly et al. 2007, 2008 in prep) is a redshift survey undertaken in the 1.7 deg<sup>2</sup> COSMOS field (Scoville et al. 2007a). The observations are carried out with the VLT using VIMOS, a multi-slit spectrograph. In zCOSMOS-bright a magnitude selection  $I_{AB} < 22.5$  has been applied to select galaxies in the redshift range up to  $\sim 1.4$ . The final sampling rate of the zCOSMOS-bright survey should be a uniform 60-70%. This paper is based on the first 10,000 spectra, which have a rather non-uniform sampling pattern, 30% on average [see the Figure with the 10k zCOSMOS sampling in Lilly et al. (2008 in prep)]. This sample of all spectra yields to the so-called “10k sample” of galaxies with only secure redshifts.

Thanks to the high-quality multi-wavelength photometry of the COSMOS survey (see Taniguchi et al. 2007; Capak et al. 2007), practically all galaxies in the zCOSMOS field can also have a photometric redshift. We employ the ZEBRA code in the Maximum-Likelihood mode (Feldmann et al. 2006) to calculate the full probability distribution functions  $P(z)$  and photometric redshifts [the maximum likelihood of  $P(z)$ ] of galaxies in the COSMOS field, using typically 10 COSMOS broad bands. The uncertainty in the photometric redshifts that we use in this paper is  $\sigma_z = 0.023(1+z)$  at  $I_{AB} < 22.5$ . The accuracy in photometric redshifts will further improve, when new photometric data become available (e.g. Ilbert et al. 2008; Salvato et al. 2008).

In our analysis, we complement the “10k sample” of galaxies with  $\sim 25,000 I_{AB} < 22.5$  galaxies which do not have, yet, spectroscopic redshifts, but for which photometric redshifts are available. We refer to this composite sample as the “10k+30k sample”. We additionally refer to the “40k sample” as the set of all galaxies with  $I_{AB} < 22.5$  in the area of the zCOSMOS survey. In the analysis below, we will frequently make use of mock catalogues (based on Kitzbichler & White 2007) for various tests, in which all galaxies in the “40k sample” have accurately known redshifts.

We use rest-frame absolute magnitudes of galaxies obtained using the ZEBRA code as the best fit template normalised to each galaxy photometry and best available redshift (spectroscopic or photometric, Oesch et al. in prep). For the galaxies with only photometric redshift, a prior which requires  $M_B$  to be in the range between -13 and -24 mag is imposed.

Stellar masses  $M_*$  are obtained from fitting stellar population synthesis models to the multicolour spectral energy distribution (SED) of the observed magnitudes (see Bolzonella et al. in prep; Pozzetti et al. in prep). In this work, we use stellar masses calculated using the Bruzual & Charlot (2003) libraries, with the Chabrier initial mass function (Chabrier 2003). The star formation history (SFH) is assumed to decrease exponentially with a time scale  $\tau$ , where  $0.1 < \tau < 30$  Gyr. The Calzetti et al. (2000) extinction law was used with  $0 < A_V < 3$  and solar metallicities. The final stellar mass is obtained by integrating the SFH over the galaxy age and subtracting from it the so called “return fraction”, which is the mass of gas processed by stars and returned to the interstellar medium during their evolution. The stellar masses are calculated using the best available redshifts for each galaxy.

##### 4.2. The choices to measure the density field with zCOSMOS

Given the diversity of the scientific applications of the density field reviewed above, we have produced a large variety of environment measures that are appropriate for different applications. In the following text we discuss the particular choices used for the measurement of the zCOSMOS density field. For practical purposes, we use the symbol  $\rho$  for all types of densities.

#### 4.2.1. Tracer galaxies: flux limited or volume limited

For the 10k zCOSMOS overdensity reconstructions, all galaxies within the zCOSMOS region with  $I_{AB} < 22.5$  are used as possible tracer galaxies. Galaxies with high confidence redshift class ( $\text{flag} \geq 1.5$ ) and the broad-line emitters with high confidence redshift class ( $\text{flag} \geq 10+1.5$ ) are counted as one object at the spectroscopic redshift (Lilly et al. 2008 in prep). Up to  $z \sim 1$ , we do not detect a significant dependence of the assigned redshift class on the type of a galaxy. For the rest of galaxies within the zCOSMOS survey limits we use the ZADE-modified ZEBRA photometric redshift output. For the few galaxies without a photometric redshift estimate, we use the ZADE-modified  $N(z)$  distribution of all galaxies in the fields as initial  $P(z)$ , normalised to unity within the redshift interval  $0 < z < 1.4$  (only a negligible fraction of galaxies with high confidence redshift class has a redshift  $z > 1.4$ ). For the few QSOs with a low confidence redshift we use the same ZADE-modified  $N(z)$  distribution to be their probability function, but normalised to  $f_{QSO}$ , which is the fraction of the broad-line objects with high-confidence class below  $z = 1.4$  in the sample of the broad-line objects with high-confidence class detected at all redshifts. For the 10k zCOSMOS sample,  $f_{QSO} = 0.43$ .

In summary, we use spectroscopic redshift information of galaxies with a spectroscopic redshift reliability  $> 99.2\%$  (which make about 85% of the spectroscopic sample), combining these with the ZADE-modified photometric redshifts for all of the galaxies either without secure redshift or those not yet observed spectroscopically.

We construct three different samples of tracer galaxies to measure the zCOSMOS over-density field. For the “flux limited sample”, all galaxies within the zCOSMOS region with  $I_{AB} < 22.5$  are used as tracer galaxies. In total, there are 33,211 such galaxies, of which 8341 have a reliable spectroscopic redshift. In addition, we define two volume limited samples of tracer galaxies, which should ideally include the same galaxies at every redshift. Understanding of galaxy evolution does not run deep enough to provide a recipe of galaxy evolution which includes all physical processes for every single galaxy (e.g. star formation episodes of various activity and merging of galaxies). Therefore, to constrain the volume limited samples, we just take into account a passive evolution of galaxies of one magnitude per unit redshift interval, which should on average account for most of the evolution for the majority of galaxies. The two volume samples satisfy the criteria  $M_B \leq -19.3 - z$  and  $z \leq 0.7$ , and  $M_B \leq -20.5 - z$  and  $0.4 < z \leq 1.0$ . To include galaxies with only photometric redshifts in the volume limited samples we use their maximum likelihood redshift and the  $M_B$  magnitude at the same redshift. However, in the density field reconstruction, we use the  $P_{ZADE}(z)$  distribution of these galaxies. Galaxies without photometric redshift or  $M_B$  are not used to construct the volume limited samples of tracer galaxies. The defined volume limited samples are complete samples, and they are selected to be the largest possible samples at these redshifts.

#### 4.2.2. Filter $W$ and smoothing length $R$

Starting from the work of Dressler (1980), when studying the galaxy properties as a function of their environment, it is common to project the tracer galaxies within some velocity interval, and then estimate the surface density. The main advantage of using the projected distances instead of the full three dimensional distances is to minimise the effects of peculiar velocities. The aperture, perpendicular to  $z$ , within which the environment is measured can be of fixed or adaptive size. Dressler (1980) for example used the projected distance to the 10th nearest neighbours to define a rectangular aperture.

Following the adopted formalism to describe the density field (equation 1), the filter  $W$  in this approach is:

$$W(|\mathbf{r} - \mathbf{r}_i|; D_p) = \begin{cases} \frac{1}{\pi D_p^2} P_{i,ZADE}(z \pm \delta z) & \text{if } |r_p - r_{i,p}| \leq D_p, |z_i - z| \leq \delta z \ (\delta z = 1000 \text{ km s}^{-1}) \\ 0 & \text{otherwise.} \end{cases} \quad (4)$$

This smoothing kernel is of cylindrical shape, with a radius of  $D_p$  in the RA-DEC plane and a length of  $\pm \delta z$  along the line of sight. The distance  $|r_p - r_{p,i}|$  is measured between the point where we are reconstructing the density field and the individual tracer galaxy projected to the redshift of that point. The  $P_{i,ZADE}(z \pm \delta z)$  is the integrated probability of the tracer galaxy to be within the  $z \pm \delta z$  interval. For galaxies with spectroscopic redshift within this interval  $P_{i,ZADE}(z \pm \delta z) = 1$ . We use the interval  $\delta z$  given by distance of  $\pm 1000 \text{ km s}^{-1}$  to the redshift  $z$  of the point where the density field is measured. Varying  $\delta z$  by  $\pm 500 \text{ km s}^{-1}$  around the chosen value of  $1000 \text{ km s}^{-1}$  does not make a significant difference.

Using the spatial filter  $W$  given in equation 4, we measure the density field at the positions of galaxies and on a regularly spaced grid. For the former, we include the central galaxy into the counts of objects, if this galaxy passes the criterion to be a tracer galaxy.

We use both fixed and adaptive apertures to estimate the density at a galaxy position. We define the adaptive aperture as the projected distance to the  $N$ th nearest neighbour  $D_N$ , excluding the central galaxy from the nearest neighbours search, but including it again when estimating the density. For the measurement on a grid we use the adaptive projected scale  $D_p = D_N$  defined by the distance to the  $N$ th nearest neighbour. Given that we are working also with the probability functions (and therefore fractional objects), in practice we measure the adaptive aperture

defined by the distance to the Nth nearest neighbour as the minimum distance for which  $\Sigma_i P_{i,ZADE}(z \pm \delta z) \geq N$ . This is valid for both estimates of the density centred on a galaxy and on a grid point.

Some of the previous studies of the galaxy evolution as a function of their environment are based on the density field reconstructed using the three dimensional Gaussian filter (e.g. Cucciati et al. 2006). To enable a proper comparison with such results, we also use a Gaussian filter to reconstruct the density field on scale  $R_G$  at the positions of zCOSMOS galaxies:

$$W(|\mathbf{r} - \mathbf{r}_i|; R_G) = \begin{cases} \frac{1}{(2\pi R_G^2)^{(3/2)}} P_{i,ZADE}(z_i) \exp\left[-\frac{1}{2}\left(\frac{\mathbf{r}-\mathbf{r}_i}{R_G}\right)^2\right] & \text{if } |\mathbf{r} - \mathbf{r}_i| \leq R_G \\ 0 & \text{otherwise,} \end{cases} \quad (5)$$

The  $|\mathbf{r} - \mathbf{r}_i|$  is a three dimensional separation between positions of a tracer galaxy and a galaxy where the density is being evaluated. If the central galaxy belongs to the sample of tracer galaxies used, it is also included in the counts.

For the biasing analysis (Kovač et al. a, in prep), we use a different scheme to reconstruct the over-density field. We want to compare the overdensity field traced by galaxies to the underlying matter overdensity, and therefore we need the overdensity field estimated on the same scale as the mass overdensity as available in the literature. Thus we use the spherical top-hat filter to reconstruct the density field of galaxies:

$$W(|\mathbf{r} - \mathbf{r}_i|; R_{TH}) = \begin{cases} \frac{1}{\frac{4}{3}\pi R_{TH}^3} P_{i,ZADE}(z_i) & \text{if } |\mathbf{r} - \mathbf{r}_i| \leq R_{TH} \\ 0 & \text{otherwise,} \end{cases} \quad (6)$$

where  $R_{TH}$  is the smoothing scale of the top-hat filter. Here,  $|\mathbf{r} - \mathbf{r}_i|$  is a three dimensional distance between a tracer galaxy and a point where the density is being estimated. An obvious shortcoming of this reconstruction is that it is affected by peculiar motions. We include this into consideration for the biasing analysis.

When the smoothing length  $R$  of a filter  $W$  is defined using the projected distances (as in Equation 4) we will denote the reconstructed overdensity with  $\delta_p$ . In the case when  $R$  is defined using the three dimensional distance (as in Equations 5 and 6), we will denote the reconstructed overdensity with  $\delta$ .

#### 4.2.3. Weighting $m_i$ of galaxies

In addition to the number overdensity reconstruction, we also calculate the B-band luminosity and stellar mass  $M_*$  weighted densities. Following equation 1, these three types of reconstructed environment correspond to the cases of  $m_i = 1$ ,  $m_i = L_B$  and  $m_i = M_*$ , respectively. We assume that the physical properties of galaxies are constant, i.e. they do not change along redshift with  $P_{ZADE}(z_i)$ .  $L_B$  and  $M_*$  are estimated at the best available redshift for each galaxy.

Weighting each galaxy with its physical property will lead to a galaxy density field still mainly determined by the spatial distribution of galaxies, with some additional discrimination based on the properties of galaxies. For example, for the same number of galaxies in two identical apertures, the measured number density will obviously be the same, while weighting galaxies with their  $L_B$  or  $M_*$  will add a finer differentiation between the measured densities.

A shortcoming of the density estimate with  $m_i \neq 1$  is that an obtained relation between galaxy properties and environment can contain some degree of correlation between the studied galaxy property and the property of the galaxy used to weight the galaxy counts for the density reconstruction. This is particularly pertinent when including the central galaxy itself in the measurement of the environment. For example, the colour-density relation will become (artificially) more significant when using  $M_*$ -weighted overdensities compared to the number overdensities (see Cucciati et al. in prep), and the differences between the stellar mass functions in the overdense and underdense regions will appear more pronounced (see Bolzonella et al. in prep). Nevertheless,  $m_i \neq 1$  weighting can be useful in defining a physically better motivated density estimator.

#### 4.3. Estimating mean density

To convert the density to an overdensity an estimate of the average density is required. Typically, galaxies in the survey itself are used to define the mean density, a value which is supposed to be valid in the whole Universe (at a given redshift). Therefore one needs to assume that these surveys are a fair sample of the Universe.

There are various ways to determine the mean density of a survey. One of the commonly used methods is smoothing the observed number distribution of the tracer galaxies along redshift, or fitting this distribution with some assumed functional form. Sometimes only the pure number density of objects in some redshift intervals is used, but in this case a part of the true variations in the overdensity with redshift will be washed away. The other commonly used method is deriving mean densities of galaxies from the galaxy luminosity function, in which case the redshift evolution of the luminosity function needs to be modelled. We use here a non-parametric treatment of the luminosity function approach.

We use the full population of tracer galaxies from the zCOSMOS survey (selected from the 10k+30kZADE sample) to define the mean volume density as a function of redshift. For each galaxy, we first calculate the maximum volume  $V_{max}$  in which this galaxy could be detected in the zCOSMOS survey, including for completeness an assumed passive evolution of  $\Delta m = \Delta z$  mag. In the next step the contribution of this galaxy to the density in each redshift bin, up to  $z_{max}$  is calculated as  $\Delta V(z)/V_{max}$ , where  $\Delta V(z)$  is the volume of the individual redshift bins.  $z_{max}$  is the maximum redshift up to which a galaxy of a given luminosity could be detected in a  $I_{AB} < 22.5$  survey;  $V_{max}$  is the volume of



the zCOSMOS survey up to redshift  $z_{max}$ . This is carried out for every tracer galaxy and then the contribution of all galaxies is summed to obtain  $N(z)$ . We present the  $N(z)$  distributions for the three samples of the zCOSMOS tracer galaxies in Figure 2. Similarly, one can calculate also the luminosity and stellar mass weighted number of objects by simply weighting  $\Delta V(z)/V_{max}$  contributions by  $L_B$  and  $M_*$ , respectively.

As desired, the procedure outlined above introduces a smoothing in the very peaky observed distribution of objects, as it can be seen in Figure 2. With respect to a more standard smoothing on the observed  $N(z)$  distribution, it has the advantage of not requiring any assumption on the smoothing length. The kernel in this smoothing procedure is of quadrilateral shape, where one side is defined by the distance between  $z_{min}$  and  $z_{max}$ , and the vertical sides are given by  $\Delta V(z)/V_{max}$  at  $z_{min}$  and  $z_{max}$ . The remaining side of this kernel is curved, defined by  $\Delta V(z)/V_{max}$  in redshifts between  $z_{min}$  and  $z_{max}$ . The exact shape of the kernel depends on  $I_{AB}$  of the individual galaxy. Due to the curved side of the kernel, a large number of galaxies at  $z \sim 0.85$  produces a somewhat overestimated  $N(z)$  above redshift of 1. The produced  $N(z)$  distributions using the spectroscopic redshifts or only maximum probability redshifts for the same group of objects are almost identical.

Finally, we obtain the mean density  $\rho_m(z)$  by normalising  $N(z)$  or its weighted counterparts by the “volume” in which  $N(z)$  is estimated. When the density is calculated using the three dimensional distances, this is obtained dividing  $N(z)$  by the volume of the zCOSMOS survey in a redshift bin centred at redshift  $z$  of that galaxy (or a grid point). To obtain the surface mean density we first integrate  $N(z)$  in the interval of  $\pm 1000 \text{ km s}^{-1}$  centred on the redshift of a galaxy or a grid point of interest to obtain the corresponding number of objects, which we afterwards divide by the zCOSMOS area.

#### 4.4. Other issues - edge effects

For all the different types of the density estimators, the effect of the edges of the survey on the estimated density is to artificially lower the density, since galaxies are not detected outside of these edges. One of the ways to avoid this is to simply exclude all (grid) points at which the aperture size is larger than the distance to the nearest edge of the survey. However, in the case of a density estimated using the adaptive aperture, this approach will bias the density estimator by excluding regions of the lower density (larger adaptive aperture) in larger proportion than the denser regions (smaller adaptive aperture).

A common way to correct for the edge effects is to scale the measured density with the fraction of the aperture which lies within the geometrical limits of the survey, assuming that the tracer galaxies in the part of the cell within and outside of the survey limits are distributed in the same manner.

For the adaptive density estimator the criteria to define the aperture close to the edges of the survey are nevertheless still affected by the edge. For example, in the case that the aperture is defined by the distance to the  $N$ th nearest neighbour, only galaxies within the survey limits will be used to define this distance. Effectively, for the same density, the smoothing length will be larger for the points close to the edges than for the points within the survey. This would artificially lower the densities near the edge due to the greater smoothing. We tested an algorithm in which the number of required neighbours is lowered close to the edges, according to the fraction of the volume within the survey limits. However, based on the tests on the mock catalogues, we find that correcting the densities at the points close to the survey limits by simply scaling the density by the fraction of the volume (area) within the survey limits works better, and is certainly much easier to implement.

For all types of the density reconstruction we therefore simply define the edge-corrected density-estimate using the following equation:

$$\rho_c = \rho/f \quad (7)$$

where  $\rho$  is estimated using equation 1 and  $f$  is the fraction of the adopted aperture that lies within the survey region. Depending on the scientific goals, one can also then exclude points with low values of  $f$ , if desired.

### 5. TESTING THE RECONSTRUCTION METHOD ON MOCK CATALOGUES

We use mock catalogues to assess the performance of the density field estimator based on the combination of galaxies with the spectroscopic and ZADE-modified photometric redshifts when applied on the 10k zCOSMOS survey. The mock catalogues for the zCOSMOS survey are extracted from the lightcone-mock catalogues described in Kitzbichler&White (2007). These lightcones are based on the dark matter N-body Millenium Simulation run (Springel et al. 2005) with  $\Omega_m = 0.25$ ,  $\Omega_b = 0.045$ ,  $h = 0.73$ ,  $\Omega_\Lambda = 0.75$ ,  $n = 1$  and  $\sigma_8 = 0.9$ . The semi-analytic galaxy modelling that is applied to the mock catalogues is described in Kitzbichler&White (2007). Essentially, it follows the model of Croton et al. (2006) as updated by de Lucia & Blaizot (2007). The only change is in the dust model, developed to better match the observations of the mass functions at higher redshifts (Kitzbichler&White 2007). There are 24 independent mock catalogues of an area  $1.4^\circ \times 1.4^\circ$  and  $z \lesssim 7$ , with a flux limit  $r \leq 26$  mag. We use 12 of these mocks, randomly chosen, to perform various tests.

The mocks are used in the following way. All mocks are cut to match the exact zCOSMOS area and redshift limits. We define the “parent” catalogue (equivalent to the 40k catalogue,  $I_{AB} < 22.5$ ), in which we assume all tracer galaxies in the zCOSMOS volume have a high quality spectroscopic redshift, and the “observed” catalogue, in which about 10,000 galaxies have spectroscopic redshifts and the rest of the tracer galaxies have only photometric redshifts (analogous to the 10k+30kZADE catalogue in the real data). The distribution of objects with the spectroscopic redshifts in the observed catalogues is modelled (see Knobel et al. in prep) to resemble that of the true 10k zCOSMOS catalogue (Lilly et al. 2008 in prep).

In the mock catalogues, we model the photometric redshift probability function  $P(z)$  as a Gaussian of dispersion  $\sigma_z$  depending on the selection  $I_{AB}$  magnitude. For galaxies with  $I_{AB} < 22.5$  mag we use  $\sigma = 0.023(1+z)$  for the purpose of the simulations. Galaxies are randomly displaced from their true redshifts by an amount selected from this same distribution. We then apply the ZADE algorithm on those galaxies without reliable spectroscopic redshifts in the mock catalogues using  $R_{ZADE} = 5 \text{ h}^{-1} \text{ Mpc}$ . We have done a simple check of the robustness of our results with respect to the functional form of the probability function by randomly assigning actual probability functions, obtained from ZEBRA for the real zCOSMOS galaxies, to the galaxies in the mock catalogue. Our results did not change significantly. The shape of the ZADE-modified  $P_{ZADE}(z)$  is determined mostly by the neighbouring galaxies and not by its initial form.

For the test on the mock catalogues, the (over)density field is calculated on a grid equally spaced in the angular units  $\Delta RA = \Delta DEC = 2$  arcmin and in the redshift  $\Delta z = 0.002$ . The density  $\rho$  in the individual grid points is estimated using equation 4, with the aperture defined by the distance to the  $N$ th nearest neighbours  $D_{p,N}$ . As we mention earlier, because we are also work with “fractional” objects, in this reconstruction we count the number of objects until  $\sum_i P_i(\Delta z) \geq N$ .

To obtain overdensities, the  $\rho$  estimate in the individual grid points is divided by  $\rho_{mean}(z)$ . In this way, the reconstructed measure of environment is given in the units of  $1 + \delta_p = \rho / \rho_{mean}$  (equation 2). For the individual mock catalogues,  $\rho_{mean}(z)$  is obtained from the smooth number distribution  $N(z)$  of the full 40k sample of tracer galaxies. We obtain the smooth  $N(z)$  distributions separately in each mock to closely resemble the uncertainties in  $\rho_{mean}(z)$  arising from the limited volume of the real survey.

We present here only the number overdensities, obtained using  $m_i = 1$  for all the tracer galaxies. The tracer galaxies are selected from the flux limited sample of galaxies. In the following plots, the survey area is limited to the central  $0.8 \times 0.8$  degrees in right ascension and declination to minimise the edge effects.

Figure 3 presents a comparison of the 10k+30kZADE “observed” and the 40k “parent” overdensities for the individual grid points, using the distance to the 10th nearest neighbour to obtain densities. The green line represents the median for the 10kspec+30kZADE observed, the red lines correspond to the 25th and 75th percentiles for the 10kspec+30kZADE observed overdensities. Binning is done as a function of parent overdensity. Obviously, the ZADE method is not perfect - it slightly overestimates the density in the most underdense regions, and it underestimates the density in most overdense regions, no doubt because of residual smearing of the initial  $P(z)$ . However, the reconstructed overdensity reproduces the parent overdensity without a significant systematic effect in the majority of regions, within the errors. This is shown in Figure 4. In all the three panels of Figure 4 we present a difference between the observed 10k+30kZADE and the parent 40k overdensities for the individual grid points, plotted as a function of the observed overdensity. The density field is reconstructed using three different adaptive apertures defined by the distance to the 5th, 10th and 20th nearest neighbour. Note that due to the ZADE approach we can compare overdensities obtained in the apertures defined by the same  $N$  (number of nearest neighbours) in the “parent” and “observed” catalogues since they both contain same total number of objects.

Based on the difference between the 25th and 75th percentiles, the error (statistical scatter) in the reconstructed overdensities using the ZADE method is roughly  $0.1 - 0.15$  dex in  $1 + \delta_p$ . It is clear that the error on the reconstructed overdensity gets smaller when using a larger number of neighbours, i.e. the density measured at larger apertures. Depending on the scientific goal, one has to balance between the smoothing scale and the statistical error on the reconstructed overdensity. The presented statistical errors include only those uncertainties arising from the fact that we are dealing with a population of galaxies with very different qualities of their measured redshifts (i.e. 10k galaxies with spectroscopic redshifts and 30k galaxies with the ZADE modified photometric redshifts). We did not include any errors arising from the uncertainties in the spectroscopic redshift or in the measured physical property. Also, these errors do not account for any differences between the 40k overdensities and the true matter overdensities. If we redo the presented comparison using the full survey area, and not only the inner part, the median and lower and upper quartiles in Figures 3 and 4 remains almost unchanged. For example, in Figure 3 there is an indication for the larger underestimation of the most overdense regions.

Figure 3 and Figure 4 are obtained by using one mock catalogue. In Figure 5 we present the difference between the observed and parent overdensities as a function of the observed overdensities for all 12 mock catalogues. The errors (i.e. the 25th and 75th percentiles of the difference between the observed and parent overdensity) at a given observed overdensity are similar for all the individual mock catalogues (and we do not show them in Figure 5). The errors in Figure 4 can therefore be taken as a reference for the errors in the observed overdensities, when using this particular method of the reconstruction of the density field.

We have chosen to present the errors on the reconstructed density field for this particular method (projected nearest neighbour and flux limited tracer galaxies) as the majority of our studies of galaxy properties are based on the density field obtained by using equation 4 and the apertures probed by this reconstruction method are smallest. We have carried out similar tests to obtain the uncertainties on the reconstructed overdensity when centred on a galaxy, using both fixed and adaptive apertures, following equation 4, and flux and volume limited tracer galaxies, weighting them with  $m_i = 1$ ,  $m_i = L_B$  and  $m_i = M_*$ . The statistical errors are comparable to the presented errors for the adaptive apertures defined by the same number of neighbours as discussed here and the fixed apertures starting from  $3 \text{ h}^{-1} \text{ Mpc}$ .

## 6. THE 10K ZCOSMOS OVER-DENSITY FIELD

### 6.1. Reconstructed environments of the zCOSMOS 10k galaxies

We present here the reconstructed environments of the 10k zCOSMOS galaxies obtained following the choices presented in Subsection 4.2. We discuss the obtained dynamical range, the dependence on the chosen aperture and

on the weighting function  $m_i$  of overdensity values quantified following equation 4, where the overdensity is estimated centred on a galaxy. The apertures are defined by projecting galaxies within  $\pm 1000 \text{ km s}^{-1}$ , and we omit direct reference to this projection in the following text.

We obtain the broadest dynamical range of reliably reconstructed local environments of the 10k zCOSMOS sample of galaxies by using the apertures defined by the distance to the 5th nearest neighbour in the flux limited sample of tracer galaxies. Based on the tests on the mock catalogue, 5 is the smallest number of neighbours which can be used to reliably reconstruct density at all redshifts probed. When using the larger number of objects to define the aperture (e.g. 10 or 20), both the most overdense and underdense regions are smoothed out, particularly the most dense ones which have a smaller physical size.

When using the volume limited samples of the tracer galaxies, the distance to the Nth nearest neighbour is equal to or larger than the distance when using the flux limited sample of tracer galaxies. Therefore, the obtained overdensities with the volume limited samples of tracer galaxies are also smoothed with respect to the overdensities reconstructed with the flux limited sample of tracer galaxies.

The distances to the 5th nearest neighbour used to define the aperture for the reconstruction of the density centred at a zCOSMOS galaxy for a set of  $\log(1 + \delta_p)$  values are presented in Figure 6, for all three samples of tracer galaxies. Rescaling this plot one can easily obtain the distances for the other values of  $N$ , since it will vary as  $(N + 1)^{(1/2)}$ .

If we use fixed apertures, the smallest scale at which we are able to reliably reconstruct environments of the 10k zCOSMOS galaxies is about  $3 \text{ h}^{-1} \text{ Mpc}$  (based on the tests on the mock catalogues), using the density estimate given by Equation 4. On this and larger scales, the dynamical range of the overdensities is smaller than when using the adaptive approach. For example, in the redshift range  $0.4 < z \leq 0.7$  where we are complete for both  $M_B < -19.3 - z$  and  $M_B < -20.5 - z$  samples of tracer galaxies, the local environments of the 10k zCOSMOS galaxies are estimated using adaptive apertures smaller than or equal to  $3 \text{ h}^{-1} \text{ Mpc}$  for 94%, 88% and 62% galaxies for the flux,  $M_B < -19.3 - z$  and  $M_B < -20.5 - z$  volume limited samples of tracer galaxies respectively. The main point to be taken is that when using the fixed aperture to measure environments we are not able to differentiate between the most overdense regions that can be reconstructed at the adaptive scales.

The ranges of overdensities discussed above are obtained by weighting tracer galaxies with  $m_i = 1$ . There is a good correlation between the number overdensities and the  $L_B$  and  $M_*$  weighted overdensities, because all are primarily set by the number of objects. However, the most overdense regions become even more overdense when using both  $m_i = L_B$  and  $m_i = M_*$ , allowing even finer differentiation of the most overdense regions. When using the  $M_*$  weighted counts of galaxies the dynamical range of overdensities is broader than when using the number or  $L_B$  weighted galaxy counts. As an example, in Figure 7 we compare a subset of differently  $m_i$ -weighted reconstructed overdensities using the  $M_B < -19.3 - z$  tracer galaxies in  $0.4 < z \leq 0.7$ , and aperture defined by the 5th nearest neighbour. Two effects are responsible for the observed scatter: the noise of the mapping between the number of galaxies and their  $L_B$  luminosities or stellar masses  $M_*$ , and different luminosity (Zucca et al. in prep) or stellar mass (Bolzonella et al. in prep) functions in different environments.

Many of these effects can be seen in Figures 8 and 9, where we present the histogram distributions of overdensities reconstructed around the 10k zCOSMOS galaxies. The overdensities are reconstructed in the apertures defined by the 10th nearest neighbour (Figure 8) and by the fixed scale of  $5 \text{ h}^{-1} \text{ Mpc}$  (Figure 9), with three types of tracer galaxies:  $I_{AB} < 22.5$  (left panels),  $M_B < -19.3 - z$  (middle panels) and  $M_B < -20.5 - z$  (right panels) and three types of weighting:  $m_i = 1$  (top row panels),  $m_i = L_B$  (middle row panels) and  $m_i = M_*$  (bottom row panels).

The advantage of the use of the volume limited sample is that, at every redshift, we are using the same type of objects to define the environment, even though the properties of these tracers can slowly change with redshift due to effects of evolution, which we cannot (yet) take out completely. The number density of these tracer galaxies is roughly constant, thus the Poisson noise and smoothing scale (if relevant) in the estimated density is on average the same at all redshifts.

On the other hand, when selecting galaxies in the total flux limited sample, the number of available tracers is larger, and one can reliably reconstruct environments on smaller scales than when using the volume limited sample. This can be critical for studying galaxy properties as a function of environment. However, different populations of galaxies will be used to define the environment at different redshifts and the typical smoothing scale will change with redshift in the adaptive approach. If using the fixed scale, systematically a different number of objects will be used to measure the environment at different redshifts and therefore the noise component in the estimate will be different at different redshifts. Normalisation to the mean overdensity (at a redshift of consideration) can overcome some of these effects.

## 6.2. Cosmographical tour of the 10k zCOSMOS survey

The global picture of the LSS structures traced by the 10k zCOSMOS galaxies is obtained by the reconstruction of the density field on the grid filling the zCOSMOS volume. For the zCOSMOS data the overdensity is reconstructed on a regular grid with spacing of  $1 \text{ h}^{-1} \text{ Mpc}$  in all three directions (along RA, DEC and  $z$  axis). All tracer galaxies within  $\pm 1000 \text{ km s}^{-1}$  are first set to the redshift of the grid point, and then used to obtain the projected distance to the 5th, 10th and 20th nearest neighbour (as for the mocks). The presented overdensity field is the projected surface overdensity field  $\delta_p$ , and the values of the full three dimensional overdensity field  $\delta$  at the same smoothing scale  $R$  would be larger,  $1 + \delta = (1 + \delta_p)^{(3/2)}$ . The overdensity field reconstructed in this way is not suited for the cosmological analysis, it is more a compilation of local environments as they would be experienced by an arbitrary object residing in the zCOSMOS volume. We use this overdensity field for the cosmographical tour of the zCOSMOS survey.

We first compare the distributions of overdensities reconstructed with the flux limited tracer galaxies on the grid, and at the positions of zCOSMOS galaxies, in Figure 10. The number of grid points is scaled to match the number of zCOSMOS galaxies with a high quality redshift in  $0.1 < z < 1$ . The smoothing of the overdensity structures is clearly visible in both the overdense and underdense tails when comparing the overdensity values reconstructed using the apertures defined by the 20th with respect to the 5th nearest neighbour, as might be expected. The most underdense regions seen on the grid are more underdense than the lowest  $1 + \delta_p$  values obtained centred on galaxies. The peak in distribution of overdensities at positions of galaxies is also shifted towards positive overdensity values [by  $\log(1 + \delta_5) \sim 0.5$  and  $\log(1 + \delta_{20}) \sim 0.4$ ] with respect to the overdensity field reconstructed on the grid points. Again, the distribution of overdensity values on the grid does not represent the universal volume distribution of overdense and underdense regions. In Kovač et al. (a, in prep), we will present the distribution of overdensity values obtained from the full three dimensional density reconstruction on the fixed scale.

A visual representation of the zCOSMOS overdensity field is presented in Figures 11, 12 and 13. For these presentations we use the overdensity field reconstructed on scales defined by the distance to the projected 5th nearest neighbour in the sample of flux limited tracer galaxies. Note that these imply that the actual smoothing scale is increasing with redshift (see Figure 6), and that different populations of galaxies are used in different redshifts to reconstruct the overdensity field. However, using the smoothing scale defined by the 5th nearest neighbour in the flux limited sample we are able to obtain the broadest possible dynamical range of the overdensity field and to preserve at best the variety of the structures in the zCOSMOS survey. As Strauss & Willick (1995) point out, a flux limited redshift survey "...is useful for qualitative and cosmographical description of the structures that are seen, and in some sense shows the maximum amount of information in the redshift survey".

The reconstructed overdensity field, presented in Figure 11, shows structures in a large range of comoving scales covering a spectrum of different overdensities at all redshifts reliably probed by the 10k zCOSMOS survey. Galaxies are distributed into cluster-like structures, surrounded by empty, void-like regions up to  $z = 1$ . A few points should be noted. First, the increased smoothness and extension of the structures in the overdensity field towards higher redshift is an artefact of the increased smoothing scale with redshift. Second, for the smallest scale structures the imprint of the filter  $W$  used is also clearly visible, especially in Figure 11. Even though sampling in the zCOSMOS field is not uniform, the resolution of similar structures is the same, given that we use ZADE to take into account galaxies without spectroscopic redshift and keep their position on the sky.

Figure 12 provides another view of the complex structure of this overdensity field, but compressed by a factor of  $\sim 3.5$  in redshift direction. Here, we present the LSS delineated by the isosurfaces enclosing regions with  $1 + \delta_p \geq 1.5$ , 3, 5 and 10 ( $1 + \delta \geq 1.8$ , 5.2, 11.2 and 31.6) going from the left to the right, respectively. The isosurface structures up to  $1 + \delta_p \geq 5$  are connected over the transverse comoving scales covering the full zCOSMOS area, and coherent over hundred or more comoving  $h^{-1}\text{Mpc}$  (or more than  $\Delta z \sim 0.1$ ) in the radial direction.

Three large structures dominate the zCOSMOS cosmic web at  $z \leq 1$ . These structures are located at  $z \sim 0.35$  (comoving distance  $D_c \sim 980 h^{-1}\text{Mpc}$ ),  $\sim 0.7$  ( $D_c \sim 1800 h^{-1}\text{Mpc}$ ) and  $\sim 0.85$  ( $D_c \sim 2100 h^{-1}\text{Mpc}$ ) and they correspond to the peaks already visible in the number distribution of galaxies with redshift (see Figure 2). The connectivity of the two largest high redshift structures extend over  $200 h^{-1}\text{Mpc}$  in the radial direction. Even though we are working with a flux limited sample of tracer galaxies, meaning that we are detecting only the brightest and presumably most massive galaxies, at  $z \sim 0.9$  the smoothing scale for the overdensities  $1 + \delta_p \geq 3$  are still below or slightly larger than  $1 h^{-1}\text{Mpc}$ , see Figure 6. Based on the tests on the mock catalogues, which include the selection effects of the 10k zCOSMOS survey, the existence of these huge overdense structures at high  $z$  is not an artefact of our reconstruction method. The other striking element in the zCOSMOS overdensity field is a very small number of  $1 + \delta_p \geq 3$  (and above) structures in  $0.4 \lesssim z \lesssim 0.6$  ( $1100 \lesssim D_c \lesssim 1580 h^{-1}\text{Mpc}$ ) except for an overdense sheet at  $z \sim 0.53$  ( $D_c \sim 1420 h^{-1}\text{Mpc}$ ).

Complementary to the large positively overdense structures, we identify in the zCOSMOS  $1 + \delta_p$  field also the structures enclosed by the overdensity values of  $1 + \delta_p = 0.15$  ( $1 + \delta = 0.06$ ) and  $\delta_p = 0.25$  ( $\delta = 0.13$ ) which contain only regions with  $1 + \delta_p$  lower than these (the underdense regions, Figure 13). The identified regions are at least 6.67 and 4 times less dense than the mean density, respectively. These regions with low galactic density do not show strong clustering in either the transversal (RA-DEC) or radial (redshift) direction. Also, they appear to be more homogeneously distributed over the zCOSMOS redshift range, even though they are less present in the redshift ranges of the three most overdense structures, being particularly absent at  $z \sim 0.35$  ( $D_c \sim 980 h^{-1}\text{Mpc}$ ).

Clearly, the amount of LSS in zCOSMOS field varies with redshift. Quantitatively, this cosmic variance of the observed structures is shown in the left panel in Figure 14, where we plot the fraction of the volume of the zCOSMOS survey enclosed within the isosurface structures of a given  $1 + \delta_p$  value. We split the sample in four  $\Delta z = 0.2$  slices, starting from  $z = 0.2$ . The fraction of the volume occupied by the structures with at least  $1 + \delta_p$  values is rapidly decreasing with  $1 + \delta_p$ . The two higher redshift slices are statistically more representative (they occupy larger volumes), and we see that for the slices above  $z = 0.6$  about 44% of the volume is in the structures with  $1 + \delta_p \geq 1$ , and about 10% of the survey volume is in the structures with  $1 + \delta_p \geq 3$ . The cosmic variance is particularly noticeable between the two lower redshift slices. At  $1 + \delta_p = 3$  and  $1 + \delta_p = 15$ , the volume fractions in those structures in the two lower redshift slices are different by a factor of  $\sim 3$  and  $\sim 4$ , respectively.

The fraction of galaxies residing in the isosurface overdensity structures is much higher than the volume fraction of these structures. Taking the two higher redshift slices as statistically more representative, we conclude that about 50% of the galaxies reside in structures with  $1 + \delta_p \geq 3.5$ , while about 50% of the stellar mass and about 50% of the

B-band luminosity at a given  $z$  inhabits the structures with  $1 + \delta_p \geq 4$  (three right panels in Figure 14). The overdense structures are few tens time more important in terms of the fractions of their baryonic content, than in terms of the volume fractions which they occupy.

### 6.3. Comparison to the other LSS measures

The high resolution of the zCOSMOS-bright spectra allows also to identify virialised groups of galaxies with velocity dispersion of  $\sim 250 \text{ km s}^{-1}$ . Knobel et al. (in prep) have applied the friends of friends and the Voronoi based group finding algorithms to the zCOSMOS galaxies with the high confidence redshift. In total, their optimal group catalogue contains 800 groups with at least 2 detected members up to redshift of 1 in the zCOSMOS volume. From these, 151 groups have at least 4 members detected. Tests on mocks show that the vast majority of all of the identified groups will be virialised objects.

The other tracer of the virialised structures is the hot baryonic gas detected in the X-rays. Finoguenov et al. (2007) carried out the identification of the X-ray clusters in the COSMOS field using the XMM-Newton observations. The updated catalogue, improved with new additional X-ray data and using the spectroscopic zCOSMOS redshifts, contains 218 X-ray clusters detected with high confidence (Finoguenov et al. in prep).

Guzzo et al. (2007) used projected densities (reconstructed with the photometric redshifts), X-ray surface brightness and one of the first weak-lensing convergence maps to describe the extended structure at  $z \sim 0.7$  in the COSMOS field. A comparison of the overdensities reconstructed at the positions of all zCOSMOS galaxies and of those galaxies residing in the virialised structures is presented in Figure 15. The majority of galaxies detected in the X-ray clusters or the richer optical groups reside in extremely overdense regions. The galaxies defining the poorer groups extend to much lower overdensities than the rich  $N \geq 4$  optical groups and X-ray clusters, and they almost completely avoid the most overdense regions.

In addition, in Figure 16 we present the visual comparison of the zCOSMOS overdensity field with the bound structures: X-ray clusters (left; Finoguenov et al. in prep) and zCOSMOS groups with at least 3 members (right; Knobel et al. in prep). There is an overall good correspondence of the overdense regions and the bound structures in the zCOSMOS volume. Almost none virialised structure is detected in regions with  $1 + \delta_p < 3$ .

More detailed insight into the spatial distribution of the overdense and virialised structures is presented in the panels of Figure 17. We use the same data as in the previous figure, but now the overdensity field is projected in redshift slices of  $\Delta z = 0.025$  width, starting from redshift 0.2. We use the cut of  $1 + \delta_p \geq 6.67$  to define the overdense regions, higher than in Figure 16. For a contrast, we also plot the equivalently underdense regions defined by isosurfaces with  $1 + \delta_p \leq 0.15$ . The X-ray structures and the optically defined groups with at least 3 detected members reside inside of the LSS defined by the chosen overdensity value in most of the cases in the whole redshift range  $0.2 < z < 1$ . However, there are some virialised structures which do not live in these most overdense regions. In fact, as we have already seen in Figures 15 and 16, the virialised structures trace also the less overdense regions. Moreover, the apparent overlap between some of the virialised structures and underdense regions in Figure 17 is only due to the projection effects.

### 6.4. Comparison of the 10k zCOSMOS LSS to the LSS in the mock catalogues

The overdensity field reconstructed using the galaxies detected in the zCOSMOS survey is highly complex, resembling the network of the local cosmic web up to the highest redshift  $z = 1$  probed. We compare here the zCOSMOS overdensity field to the overdensity fields in the “10k+30kZADE” mock catalogues. The mock catalogues and the density field reconstruction procedure on the mocks were discussed in Section 5. For the exact comparison of the data and the mock overdensity field, we reconstruct the overdensity field of the 10k zCOSMOS galaxies on the same grid as was used for the mock catalogues, defined by  $\Delta RA = \Delta DEC = 2 \text{ arcmin}$  and  $\Delta z = 0.002$  and using the flux limited tracers of galaxies. We did not calculate the edge corrections for all the mock catalogues (which is a very time consuming process computationally), and instead compare the overdensity fields uncorrected for edge effects for both the data and the mocks. Given that we are only interested in comparing the structures in the overdensity fields in the data with structures in the mocks, and not to draw any scientific conclusions from the distributions of the detected structures, this should not matter.

In Figure 18 we show the three dimensional distribution of the  $1 + \delta_p = 3$  isosurface in the overdensity field estimated on the angular grid of the 10k zCOSMOS galaxies and of the mock catalogues. The visual inspection of the LSS defined by the  $1 + \delta_p = 3$  isosurfaces leaves the impression that there are more large structures in the real data than in the mock catalogues.

For a quantitative comparison of the overdensity field of the real zCOSMOS and mock catalogues we implement a volume filling statistic. We calculate the fraction of the survey volume in which the overdensity value is above a given threshold. As a reference, we use the value obtained by averaging the individual statistics from the 12 mock catalogues. We use the standard deviation of the 12 mock results as an error estimate, which is dominated by the cosmic variance.

First, we compare the overall distribution of the survey volumes in structures of a given  $\delta_p$  value in the  $0.2 < z < 1$  redshift range using the overdensity field reconstructed in the apertures defined by the distance to the 10th nearest neighbour of the flux limited tracer galaxies (Figure 19, left). Even though we use the angular grid to reconstruct the density field, we count the comoving volumes (in  $[\text{h}^{-1}\text{Mpc}]^3$ ) of the individual cells to properly calculate these volume fractions. There is an excellent agreement, within  $1\sigma$  errors, between the fractions of the volumes in the isosurface structures in the data and in the average mock.

We carry out the same analysis dividing the redshift range in four intervals:  $0.2 < z < 0.4$ ,  $0.4 < z < 0.6$ ,  $0.6 < z < 0.8$  and  $0.8 < z < 1$  (Figure 19, right). While the overdensity distributions of the data in  $0.2 < z < 0.4$  and  $0.6 < z < 0.8$  redshift ranges are in relatively good agreement with the mock results, the redshift interval  $0.4 < z < 0.6$  is underdense in the data with respect to the mocks, while the situation is reversed in the redshift interval  $0.8 < z < 1$ . Obviously, at any redshift bin and at a given  $\delta_p$ , the real data are affected by the cosmic variance, and we can not see the growth in the cosmic structure over redshifts, as it is visible in the mock curves.

We follow up on this with a more detailed comparison of the distribution of “sizes” (volumes) of the structures above a given overdensity in the data and in the individual mock catalogues. We calculate the size of a structure by adding comoving volumes of the connected grid cells with overdensity above a chosen value. The grid cells need to have at least one common side (either in RA, DEC or  $z$  direction) to be considered connected. The results are presented in Figure 20 for  $1 + \delta_p \geq 3$ . The individual plots correspond to the survey volume fractions contained within the structures of at least the indicated size. It is noticeable that there is not a single mock catalogue which contains as much volume as the real data in the largest structures in  $0.2 < z < 1$ . As a check we also recalculate the same statistics for the data when using the mean density estimated following the same smoothing scheme as applied to the mocks (even though this smoothing is not ideal for the data). In this case, the difference between the data and the mocks is even larger.

Carrying the same analysis in the narrower redshift intervals we realise that the majority of this difference is accounted for by the large structure in  $0.8 < z < 1$ . Already, when we limit the redshift range to  $0.3 < z < 0.9$ , the data are not so different from the mocks. To conclude, except for the large structure in the highest redshift bin  $0.8 < z < 1$ , the fraction of the volume within the structures of a given size in the data and in the mock catalogues is in reasonable agreement. At the current state, given that there is a disagreement in only one  $\Delta z$  slice, it is difficult to say whether the large structure in  $0.8 < z < 1$  reflects only a cosmic variance, or it is an unusual object for the current cosmology.

## 7. SUMMARY

We have used the first  $\sim 10,000$  spectra from the zCOSMOS bright survey to reconstruct the density field in the survey volume up to  $z = 1$ . We use a new method for the reconstruction, which is based on the combination of the high quality spectroscopic redshifts and the ZADE-modified photometric redshifts of galaxies without spectroscopic redshifts. Our method enables us to reliably reconstruct a broader range of environments than it would be possible by using only galaxies with spectroscopic redshifts.

We use the weighted counts of tracer galaxies within various apertures to measure the galaxy environments in the zCOSMOS volume. Given the variety of the scientific applications, we carry out the reconstruction in different ways. We construct flux and volume limited samples of tracer galaxies, specify fixed and adaptive apertures (characterised by distance to the  $N$ th nearest neighbour), define three dimensional and projected distances. We weight tracer galaxies in three different ways: with unity, B-band luminosity and stellar mass.

We present in detail the density field reconstructed on the grid filling the zCOSMOS volume up to  $z = 1$ . The apertures are defined by the distance to the  $N$ th nearest neighbour (5th, 10th and 20th) projected within  $\pm 1000$  km s<sup>-1</sup> to the redshift of a point where the density is being measured. We use the flux limited tracer galaxies, as this sample of tracers allows to reconstruct the density field with the broadest dynamical range and with the greatest detail of the structures. The reconstructed zCOSMOS overdensity field consists of cluster-like structures, surrounded by void-like regions, showing a complexity of the cosmic web up to  $z \sim 1$ .

The regions in the density field enclosed by the  $1 + \delta_p \geq 3$ , or higher cutoff values, are well traced by the virialised objects in the zCOSMOS volume, i.e. X-ray clusters and optical groups with at least 3 detected members. The galaxies defining the poorer groups (with 2 or 3 detected members) are found to live also in much lower overdensities than the rich  $N \geq 4$  optical groups and X-ray clusters.

Further on, we have compared the LSS in the zCOSMOS data and in the mock catalogues. There is an excellent agreement of the fractions of the volume enclosed in structures of all sizes above a given overdensity between the data and the mocks in  $0.2 < z < 1$ . However, for the chosen  $1 + \delta_p = 3$  value, there is more volume enclosed in the large structures in the data than in any of the used mocks; we want to stress that this difference is mainly driven by the existence of a very large structure in the zCOSMOS, centred at  $z \sim 0.9$  and extending in radial direction over  $\Delta z \sim 0.2$ .

## 8. ACKNOWLEDGMENTS

This work has been supported in part by a grant from the Swiss National Science Foundation and by grant ASI/COFIS/WP3110I/026/07/0. We thank M.G. Kitzbichler and S.D.M. White for providing the mock catalogues (Kitzbichler & White 2007).

## REFERENCES

- |  |  |
|--|--|
| <p>Aragón-Calvo, M. A., Jones, B. J. T., van de Weygaert, R., &amp; van der Hulst, J. M. 2007, <i>A&amp;A</i>, 474, 315</p> <p>Bernardeau, F. &amp; van de Weygaert, R. 1996, <i>MNRAS</i>, 279, 693</p> <p>Blanton, M. R., Eisenstein, D., Hogg, D. W., &amp; Zehavi, I. 2006, <i>ApJ</i>, 645, 977</p> | <p>Blanton, M. R., Hogg, D. W., Bahcall, N. A., Baldry, I. K., Brinkmann, J., Csabai, I., Eisenstein, D., Fukugita, M., Gunn, J. E., Ivezić, Ž., Lamb, D. Q., Lupton, R. H., Loveday, J., Munn, J. A., Nichol, R. C., Okamura, S., Schlegel, D. J., Shimasaku, K., Strauss, M. A., Vogeley, M. S., &amp; Weinberg, D. H. 2003, <i>ApJ</i>, 594, 186</p> <p>Bolzonella, M. in prep.</p> |
|--|--|

- Bond, J. R., Kofman, L., & Pogosyan, D. 1996, *Nature*, 380, 603
- Bruzual, G. & Charlot, S. 2003, *MNRAS*, 344, 1000
- Calzetti, D., Armus, L., Bohlin, R. C., Kinney, A. L., Koornneef, J., & Storchi-Bergmann, T. 2000, *ApJ*, 533, 682
- Capak, P., Aussel, H., Ajiki, M., McCracken, H. J., Mobasher, B., Scoville, N., Shopbell, P., Taniguchi, Y., Thompson, D., Tribiano, S., Sasaki, S., Blain, A. W., Brusa, M., Carilli, C., Comastri, A., Carollo, C. M., Cassata, P., Colbert, J., Ellis, R. S., Elvis, M., Giavalisco, M., Green, W., Guzzo, L., Hasinger, G., Ilbert, O., Impey, C., Jahnke, K., Kartaltepe, J., Kneib, J.-P., Koda, J., Koekemoer, A., Komiyama, Y., Leauthaud, A., Lefevre, O., Lilly, S., Liu, C., Massey, R., Miyazaki, S., Murayama, T., Nagao, T., Peacock, J. A., Pickles, A., Porciani, C., Renzini, A., Rhodes, J., Rich, M., Salvato, M., Sanders, D. B., Scarlata, C., Schiminovich, D., Schinnerer, E., Scodreggio, M., Sheth, K., Shioya, Y., Tasca, L. A. M., Taylor, J. E., Yan, L., & Zamorani, G. 2007, *ApJS*, 172, 99
- Capak, P., Abraham, R. G., Ellis, R. S., Mobasher, B., Scoville, N., Sheth, K., & Koekemoer, A. 2007a, *ApJS*, 172, 284
- Caputi, K. I., Kovac, K., Bolzonella, M., Lilly, S. J., Zamorani, G., Aussel, H., Sanders, D., Bardelli, S., Bongiorno, A., Contini, T., Coppa, G., Cucciati, O., de la Torre, S., de Ravel, L., Franzetti, P., Frayer, D., Garilli, B., Iovino, A., Kampczyk, P., Kneib, J. ., Knobel, C., Lamareille, F., Le Borgne, J. ., Le Brun, V., Le Fèvre, O., Le Floc'h, E., Leauthaud, A., Maier, C., Mainieri, V., Mignoli, M., Pello, R., Peng, Y., Perez-Montero, E., Ricciardelli, E., Salvato, M., Scodreggio, M., Scoville, N., Silverman, J., Surace, J., Tanaka, M., Tasca, L., Tresse, L., Vergani, D., Zucca, E., Abbas, U., Bottini, D., Capak, P., Cappi, A., Carollo, C. M., Cassata, P., Cimatti, A., Fumana, M., Ilbert, O., Kartaltepe, J., Maccagni, D., Marinoni, C., McCracken, H., Memeo, P., Meneux, B., Oesch, P., Porciani, C., Pozzetti, L., Renzini, A., Scaramella, R., & Scarlata, C. 2008, *ArXiv e-prints*
- Chabrier, G. 2003, *PASP*, 115, 763
- Coles, P. & Jones, B. 1991, *MNRAS*, 248, 1
- Colless, M., Dalton, G., Maddox, S., Sutherland, W., Norberg, P., Cole, S., Bland-Hawthorn, J., Bridges, T., Cannon, R., Collins, C., Couch, W., Cross, N., Deeley, K., De Propris, R., Driver, S. P., Efstathiou, G., Ellis, R. S., Frenk, C. S., Glazebrook, K., Jackson, C., Lahav, O., Lewis, I., Lumsden, S., Madgwick, D., Peacock, J. A., Peterson, B. A., Price, I., Seaborne, M., & Taylor, K. 2001, *MNRAS*, 328, 1039
- Cooper, M. C., Newman, J. A., Coil, A. L., Croton, D. J., Gerke, B. F., Yan, R., Davis, M., Faber, S. M., Guhathakurta, P., Koo, D. C., Weiner, B. J., & Willmer, C. N. A. 2007, *MNRAS*, 376, 1445
- Cooper, M. C., Newman, J. A., Madgwick, D. S., Gerke, B. F., Yan, R., & Davis, M. 2005, *ApJ*, 634, 833
- Cucciati, O., Iovino, A., Marinoni, C., Ilbert, O., Bardelli, S., Franzetti, P., Le Fèvre, O., Pollo, A., Zamorani, G., Cappi, A., Guzzo, L., McCracken, H. J., Meneux, B., Scaramella, R., Scodreggio, M., Tresse, L., Zucca, E., Bottini, D., Garilli, B., Le Brun, V., Maccagni, D., Picat, J. P., Vettolani, G., Zanichelli, A., Adami, C., Arnaboldi, M., Arnouts, S., Bolzonella, M., Charlot, S., Ciliegi, P., Contini, T., Foucaud, S., Gavignaud, I., Marano, B., Mazure, A., Merighi, R., Paltani, S., Pellò, R., Pozzetti, L., Radovich, M., Bondi, M., Bongiorno, A., Busarello, G., de La Torre, S., Gregorini, L., Lamareille, F., Mathez, G., Mellier, Y., Merluzzi, P., Ripepi, V., Rizzo, D., Tempurin, S., & Vergani, D. 2006, *A&A*, 458, 39
- Cucciati, O. in prep.
- Davis, M., Faber, S. M., Newman, J., Phillips, A. C., Ellis, R. S., Steidel, C. C., Conselice, C., Coil, A. L., Finkbeiner, D. P., Koo, D. C., Guhathakurta, P., Weiner, B., Schiavon, R., Willmer, C., Kaiser, N., Luppino, G. A., Wirth, G., Connolly, A., Eisenhardt, P., Cooper, M., & Gerke, B. 2003, in Presented at the Society of Photo-Optical Instrumentation Engineers (SPIE) Conference, Vol. 4834, Society of Photo-Optical Instrumentation Engineers (SPIE) Conference Series, ed. P. Guhathakurta, 161–172
- de Lapparent, V., Geller, M. J., & Huchra, J. P. 1986, *ApJ*, 302, L1
- Delone, B. N. 1934, *Bull.Acad.Sci.USSR:Classe Sci.Mat*, 7, 793
- Dirichlet, G. L. 1850, *J. reine angew. Math.*, 40, 209
- Dressler, A. 1980, *ApJ*, 236, 351
- Feldmann, R., Carollo, C. M., Porciani, C., Lilly, S. J., Capak, P., Taniguchi, Y., Le Fèvre, O., Renzini, A., Scoville, N., Ajiki, M., Aussel, H., Contini, T., McCracken, H., Mobasher, B., Murayama, T., Sanders, D., Sasaki, S., Scarlata, C., Scodreggio, M., Shioya, Y., Silverman, J., Takahashi, M., Thompson, D., & Zamorani, G. 2006, *MNRAS*, 372, 565
- Finoguenov, A., Guzzo, L., Hasinger, G., Scoville, N. Z., Aussel, H., Böhringer, H., Brusa, M., Capak, P., Cappelluti, N., Comastri, A., Giodini, S., Griffiths, R. E., Impey, C., Koekemoer, A. M., Kneib, J.-P., Leauthaud, A., Le Fèvre, O., Lilly, S., Mainieri, V., Massey, R., McCracken, H. J., Mobasher, B., Murayama, T., Peacock, J. A., Sakelliou, I., Schinnerer, E., Silverman, J. D., Smolčić, V., Taniguchi, Y., Tasca, L., Taylor, J. E., Trump, J. R., & Zamorani, G. 2007, *ApJS*, 172, 182
- Finoguenov, A. in prep.
- Forero-Romero, J. E., Hoffman, Y., Gottloeber, S., Klypin, A., & Yepes, G. 2008, *ArXiv e-prints*
- Guzzo, L., Cassata, P., Finoguenov, A., Massey, R., Scoville, N. Z., Capak, P., Ellis, R. S., Mobasher, B., Taniguchi, Y., Thompson, D., Ajiki, M., Aussel, H., Böhringer, H., Brusa, M., Calzetti, D., Comastri, A., Franceschini, A., Hasinger, G., Kasliwal, M. M., Kitzbichler, M. G., Kneib, J.-P., Koekemoer, A., Leauthaud, A., McCracken, H. J., Murayama, T., Nagao, T., Rhodes, J., Sanders, D. B., Sasaki, S., Shioya, Y., Tasca, L., & Taylor, J. E. 2007, *ApJS*, 172, 254
- Hahn, O., Carollo, C. M., Porciani, C., & Dekel, A. 2007a, *MNRAS*, 381, 41
- Hahn, O., Porciani, C., Carollo, C. M., & Dekel, A. 2007b, *MNRAS*, 375, 489
- Hernquist, L. & Katz, N. 1989, *ApJS*, 70, 419
- Hoffman, Y. 1994, in *Astronomical Society of the Pacific Conference Series*, Vol. 67, *Unveiling Large-Scale Structures Behind the Milky Way*, ed. C. Balkowski & R. C. Kraan-Korteweg, 185–+
- Ilbert, O., Capak, P., Salvato, M., Aussel, H., McCracken, H. J., Sanders, D. B., Scoville, N., Kartaltepe, J., Arnouts, S., Le Floc'h, E., Mobasher, B., Taniguchi, Y., Lamareille, F., Leauthaud, A., Sasaki, S., Thompson, D., Zamojski, M., Zamorani, G., Bardelli, S., Bolzonella, M., Bongiorno, A., Brusa, M., Caputi, K. I., Carollo, C. M., Contini, T., Cook, R., Coppa, G., Cucciati, O., de la Torre, S., de Ravel, L., Franzetti, P., Garilli, B., Hasinger, G., Iovino, A., Kampczyk, P., Kneib, J. ., Knobel, C., Kovac, K., Le Borgne, J. F., Le Brun, V., Le Fèvre, O., Lilly, S., Looper, D., Maier, C., Mainieri, V., Mellier, Y., Mignoli, M., Murayama, T., Pello, R., Peng, Y., Perez-Montero, E., Renzini, A., Ricciardelli, E., Schiminovich, D., Scodreggio, M., Shioya, Y., Silverman, J., Surace, J., Tanaka, M., Tasca, L., Tresse, L., Vergani, D., & Zucca, E. 2008, *ArXiv e-prints*
- Kauffmann, G., White, S. D. M., Heckman, T. M., Ménard, B., Brinchmann, J., Charlot, S., Tremonti, C., & Brinkmann, J. 2004, *MNRAS*, 353, 713
- Kitzbichler, M. G. & White, S. D. M. 2007, *MNRAS*, 376, 2
- Kovač, K. a, in prep.
- Kovač, K. b, in prep.
- Knobel, C. in prep.
- Lahav, O., Fisher, K. B., Hoffman, Y., Scharf, C. A., & Zaroubi, S. 1994, *ApJ*, 423, L93+
- Le Fèvre, O., Vettolani, G., Garilli, B., Tresse, L., Bottini, D., Le Brun, V., Maccagni, D., Picat, J. P., Scaramella, R., Scodreggio, M., Zanichelli, A., Adami, C., Arnaboldi, M., Arnouts, S., Bardelli, S., Bolzonella, M., Cappi, A., Charlot, S., Ciliegi, P., Contini, T., Foucaud, S., Franzetti, P., Gavignaud, I., Guzzo, L., Ilbert, O., Iovino, A., McCracken, H. J., Marano, B., Marinoni, C., Mathez, G., Mazure, A., Meneux, B., Merighi, R., Paltani, S., Pellò, R., Pollo, A., Pozzetti, L., Radovich, M., Zamorani, G., Zucca, E., Bondi, M., Bongiorno, A., Busarello, G., Lamareille, F., Mellier, Y., Merluzzi, P., Ripepi, V., & Rizzo, D. 2005, *A&A*, 439, 845
- Lee, J. & Lee, B. 2008, *ArXiv e-prints*
- Lee, J. & Li, C. 2008, *ArXiv e-prints*

- Lilly, S. J., Le Fèvre, O., Renzini, A., Zamorani, G., Scodreggio, M., Contini, T., Carollo, C. M., Hasinger, G., Kneib, J.-P., Iovino, A., Le Brun, V., Maier, C., Mainieri, V., Mignoli, M., Silverman, J., Tasca, L. A. M., Bolzonella, M., Bongiorno, A., Bottini, D., Capak, P., Caputi, K., Cimatti, A., Cucciati, O., Daddi, E., Feldmann, R., Franzetti, P., Garilli, B., Guzzo, L., Ilbert, O., Kampczyk, P., Kovac, K., Lamareille, F., Leauthaud, A., Borgne, J.-F. L., McCracken, H. J., Marinoni, C., Pello, R., Ricciardelli, E., Scarlata, C., Vergani, D., Sanders, D. B., Schinnerer, E., Scoville, N., Taniguchi, Y., Arnouts, S., Aussel, H., Bardelli, S., Brusa, M., Cappi, A., Ciliegi, P., Finoguenov, A., Foucaud, S., Franceschini, R., Halliday, C., Impey, C., Knobel, C., Koekemoer, A., Kurk, J., Maccagni, D., Maddox, S., Marano, B., Marconi, G., Meneux, B., Mobasher, B., Moreau, C., Peacock, J. A., Porciani, C., Pozzetti, L., Scaramella, R., Schiminovich, D., Shopbell, P., Smail, I., Thompson, D., Tresse, L., Vettolani, G., Zanichelli, A., & Zucca, E. 2007, *ApJS*, 172, 70
- Lilly, S. in prep.
- Marinoni, C., Guzzo, L., Cappi, A., Le Fèvre, O., Mazure, A., Meneux, B., Pollo, A., Iovino, A., McCracken, H. J., Scaramella, R., de La Torre, S., Virey, J. M., Bottini, D., Garilli, B., Le Brun, V., Maccagni, D., Picat, J. P., Scodreggio, M., Tresse, L., Vettolani, G., Zanichelli, A., Adami, C., Arnouts, S., Bardelli, S., Bolzonella, M., Charlot, S., Ciliegi, P., Contini, T., Foucaud, S., Franzetti, P., Gavignaud, I., Ilbert, O., Lamareille, F., Marano, B., Mathez, G., Merighi, R., Paltani, S., Pellò, R., Pozzetti, L., Radovich, M., Vergani, D., Zamorani, G., Zucca, E., Abbas, U., Bondi, M., Bongiorno, A., Brinchmann, J., Buzzi, A., Cucciati, O., de Ravel, L., Gregorini, L., Mellier, Y., Merluzzi, P., Perez-Montero, E., Taxil, P., Tempurin, S., & Walcher, C. J. 2008, *A&A*, 487, 7
- Marinoni, C., Le Fèvre, O., Meneux, B., Iovino, A., Pollo, A., Ilbert, O., Zamorani, G., Guzzo, L., Mazure, A., Scaramella, R., Cappi, A., McCracken, H. J., Bottini, D., Garilli, B., Le Brun, V., Maccagni, D., Picat, J. P., Scodreggio, M., Tresse, L., Vettolani, G., Zanichelli, A., Adami, C., Arnouts, S., Bardelli, S., Blaizot, J., Bolzonella, M., Charlot, S., Ciliegi, P., Contini, T., Foucaud, S., Franzetti, P., Gavignaud, I., Marano, B., Mathez, G., Merighi, R., Paltani, S., Pellò, R., Pozzetti, L., Radovich, M., Zucca, E., Bondi, M., Bongiorno, A., Busarello, G., Colombi, S., Cucciati, O., Lamareille, F., Mellier, Y., Merluzzi, P., Ripepi, V., & Rizzo, D. 2005, *A&A*, 442, 801
- Novikov, D., Colombi, S., & Doré, O. 2006, *MNRAS*, 366, 1201
- Oesch, P. in prep.
- Owen, J. M., Villumsen, J. V., Shapiro, P. R., & Martel, H. 1998, *ApJS*, 116, 155
- Park, C., Choi, Y.-Y., Vogeley, M. S., Gott, J. R. I., & Blanton, M. R. 2007, *ApJ*, 658, 898
- Pozzetti, L. in prep.
- Romano-Díaz, E. & van de Weygaert, R. 2007, *MNRAS*, 382, 2
- Salvato, M., Hasinger, G., Ilbert, O., Zamorani, G., Brusa, M., Scoville, N., Rau, A., Capak, P., Arnouts, S., Aussel, H., Bolzonella, M., Bongiorno, A., Cappelluti, N., Caputi, K., Civano, F., Cook, R., Elvis, M., Gilli, R., Jahnke, K., Kartaltepe, J. S., Impey, C. D., Lamareille, F., Le Floche, E., Lilly, S., Mainieri, V., McCarthy, P., McCracken, H., Mignoli, M., Mobasher, B., Murayama, T., Sasaki, S., Sanders, D. B., Schiminovich, D., Shioya, Y., Shopbell, P., Silvermann, J., Smolcic, V., Surace, J., Taniguchi, Y., Thompson, D., Trump, J. R., Urry, M., & Zamojski, M. 2008, *ArXiv e-prints*
- Schaap, W. E. 2007, PhD thesis, Groningen: Rijksuniversiteit
- Schaap, W. E. & van de Weygaert, R. 2000, *A&A*, 363, L29
- Scoville, N., Abraham, R. G., Aussel, H., Barnes, J. E., Benson, A., Blain, A. W., Calzetti, D., Comastri, A., Capak, P., Carilli, C., Carlstrom, J. E., Carollo, C. M., Colbert, J., Daddi, E., Ellis, R. S., Elvis, M., Ewald, S. P., Fall, M., Franceschini, A., Gialalisco, M., Green, W., Griffiths, R. E., Guzzo, L., Hasinger, G., Impey, C., Kneib, J.-P., Koda, J., Koekemoer, A., Lefevre, O., Lilly, S., Liu, C. T., McCracken, H. J., Massey, R., Mellier, Y., Miyazaki, S., Mobasher, B., Mould, J., Norman, C., Refregier, A., Renzini, A., Rhodes, J., Rich, M., Sanders, D. B., Schiminovich, D., Schinnerer, E., Scodreggio, M., Sheth, K., Shopbell, P. L., Taniguchi, Y., Tyson, N. D., Urry, C. M., Van Waerbeke, L., Vettolani, P., White, S. D. M., & Yan, L. 2007a, *ApJS*, 172, 38
- Scoville, N., Aussel, H., Benson, A., Blain, A., Calzetti, D., Capak, P., Ellis, R. S., El-Zant, A., Finoguenov, A., Gialalisco, M., Guzzo, L., Hasinger, G., Koda, J., Le Fèvre, O., Massey, R., McCracken, H. J., Mobasher, B., Renzini, A., Rhodes, J., Salvato, M., Sanders, D. B., Sasaki, S. S., Schinnerer, E., Sheth, K., Shopbell, P. L., Taniguchi, Y., Taylor, J. E., & Thompson, D. J. 2007b, *ApJS*, 172, 150
- Shapiro, P. R., Martel, H., Villumsen, J. V., & Owen, J. M. 1996, *ApJS*, 103, 269
- Sigad, Y., Branchini, E., & Dekel, A. 2000, *ApJ*, 540, 62
- Silverman, J. submitted to *ApJ*
- Sousbie, T., Pichon, C., Colombi, S., Novikov, D., & Pogossyan, D. 2008, *MNRAS*, 383, 1655
- Strauss, M. A. & Willick, J. A. 1995, *Phys. Rep.*, 261, 271
- Taniguchi, Y., Scoville, N., Murayama, T., Sanders, D. B., Mobasher, B., Aussel, H., Capak, P., Ajiki, M., Miyazaki, S., Komiyama, Y., Shioya, Y., Nagao, T., Sasaki, S. S., Koda, J., Carilli, C., Gialalisco, M., Guzzo, L., Hasinger, G., Impey, C., LeFevre, O., Lilly, S., Renzini, A., Rich, M., Schinnerer, E., Shopbell, P., Kaifu, N., Karoji, H., Arimoto, N., Okamura, S., & Ohta, K. 2007, *ApJS*, 172, 9
- Tasca, L. in prep.
- van Breukelen, C., Clewley, L., Bonfield, D. G., Rawlings, S., Jarvis, M. J., Barr, J. M., Foucaud, S., Almaini, O., Cirasuolo, M., Dalton, G., Dunlop, J. S., Edge, A. C., Hirst, P., McLure, R. J., Page, M. J., Sekiguchi, K., Simpson, C., Smail, I., & Watson, M. G. 2006, *MNRAS*, 373, L26
- van de Weygaert, R. & Bertschinger, E. 1996, *MNRAS*, 281, 84
- Vergani, D. in prep.
- Voronoi, G. 1908, *J. reine angew. Math.*, 134, 198
- York, D. G., Adelman, J., Anderson, Jr., J. E., Anderson, S. F., Annis, J., Bahcall, N. A., Bakken, J. A., Barkhouser, R., Bastian, S., Berman, E., Boroski, W. N., Bracker, S., Briegel, C., Briggs, J. W., Brinkmann, J., Brunner, R., Burles, S., Carey, L., Carr, M. A., Castander, F. J., Chen, B., Colestock, P. L., Connolly, A. J., Crocker, J. H., Csabai, I., Czarapata, P. C., Davis, J. E., Doi, M., Dombeck, T., Eisenstein, D., Ellman, N., Elms, B. R., Evans, M. L., Fan, X., Federwitz, G. R., Fiscelli, L., Friedman, S., Frieman, J. A., Fukugita, M., Gillespie, B., Gunn, J. E., Gurbani, V. K., de Haas, E., Haldeman, M., Harris, F. H., Hayes, J., Heckman, T. M., Hennessy, G. S., Hindsley, R. B., Holm, S., Holmgren, D. J., Huang, C.-h., Hull, C., Husby, D., Ichikawa, S.-I., Ichikawa, T., Ivezić, Ž., Kent, S., Kim, R. S. J., Kinney, E., Klaene, M., Kleinman, A. N., Kleinman, S., Knapp, G. R., Korienek, J., Kron, R. G., Kunszt, P. Z., Lamb, D. Q., Lee, B., Leger, R. F., Limmongkol, S., Lindenmeyer, C., Long, D. C., Loomis, C., Loveday, J., Lucinio, R., Lupton, R. H., MacKinnon, B., Mannery, E. J., Mantsch, P. M., Margon, B., McGehee, P., McKay, T. A., Meiksin, A., Merelli, A., Monet, D. G., Munn, J. A., Narayanan, V. K., Nash, T., Neilsen, E., Neswold, R., Newberg, H. J., Nichol, R. C., Nicinski, T., Nonino, M., Okada, N., Okamura, S., Ostroiker, J. P., Owen, R., Pauls, A. G., Peoples, J., Peterson, R. L., Petravick, D., Pier, J. R., Pope, A., Pordes, R., Prosapio, A., Rechenmacher, R., Quinn, T. R., Richards, G. T., Richmond, M. W., Rivetta, C. H., Rockosi, C. M., Ruthmansdorfer, K., Sandford, D., Schlegel, D. J., Schneider, D. P., Sekiguchi, M., Sergey, G., Shimasaku, K., Siegmund, W. A., Smeed, S., Smith, J. A., Snedden, S., Stone, R., Stoughton, C., Strauss, M. A., Stubbs, C., SubbaRao, M., Szalay, A. S., Szapudi, I., Szokoly, G. P., Thakar, A. R., Tremonti, C., Tucker, D. L., Uomoto, A., Vanden Berk, D., Vogeley, M. S., Waddell, P., Wang, S.-i., Watanabe, M., Weinberg, D. H., Yanny, B., & Yasuda, N. 2000, *AJ*, 120, 1579
- Zaroubi, S., Hoffman, Y., Fisher, K. B., & Lahav, O. 1995, *ApJ*, 449, 446
- Zucca, E. in prep.



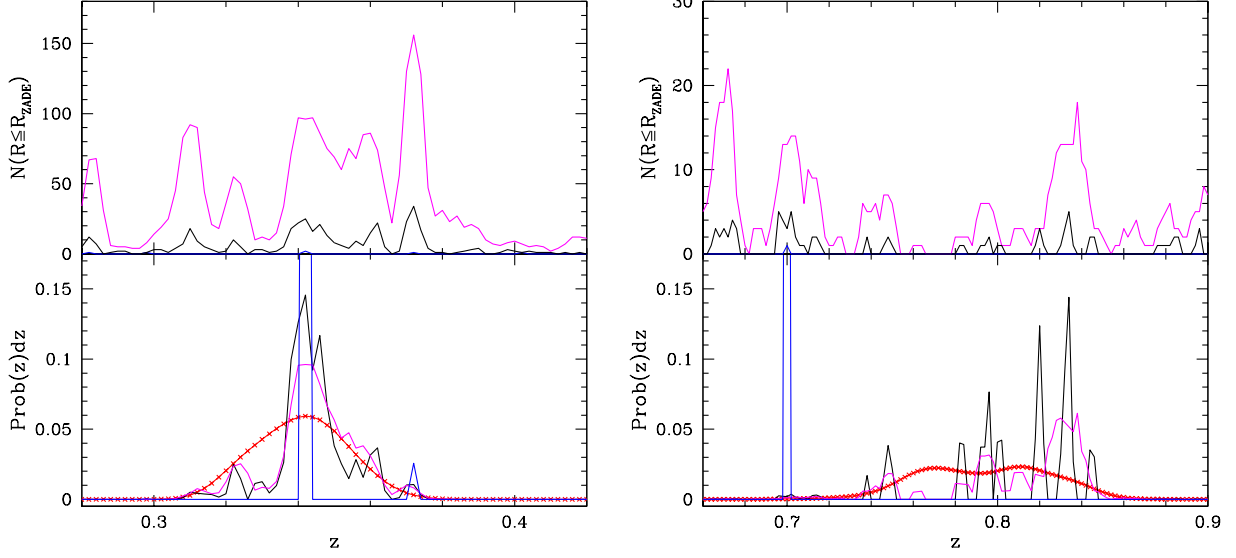


FIG. 1.— ZADE approach to modify the initial  $P(z)$ , discretised in  $\Delta z = 0.002$ . The photometric redshift probability functions are presented in the lower panels. The  $P(z)$  output from ZEBRA is presented in red and the ZADE-modified  $P_{ZADE}(z)$  are presented in blue ( $R_{ZADE} \leq 1 \text{ h}^{-1}\text{Mpc}$ ), black ( $R_{ZADE} \leq 5 \text{ h}^{-1}\text{Mpc}$ ) and magenta ( $R_{ZADE} \leq 10 \text{ h}^{-1}\text{Mpc}$ ). The number counts of objects with spectroscopic redshifts within  $R_{ZADE}$  radii at a given  $z$  are presented in the upper panels, using the same colour coding as in the lower panels. The left panel is for an object with  $I_{AB}=21.94$  mag, the right panel is for an object with  $I_{AB}=22.38$  mag. Note that the number of objects with spectroscopic redshift within  $R_{ZADE} \leq 1 \text{ h}^{-1}\text{Mpc}$  is very small, and therefore  $N(R \leq R_{ZADE}=1 \text{ h}^{-1}\text{Mpc})$  is zero at almost all  $z$  (upper panels). See text for more details.

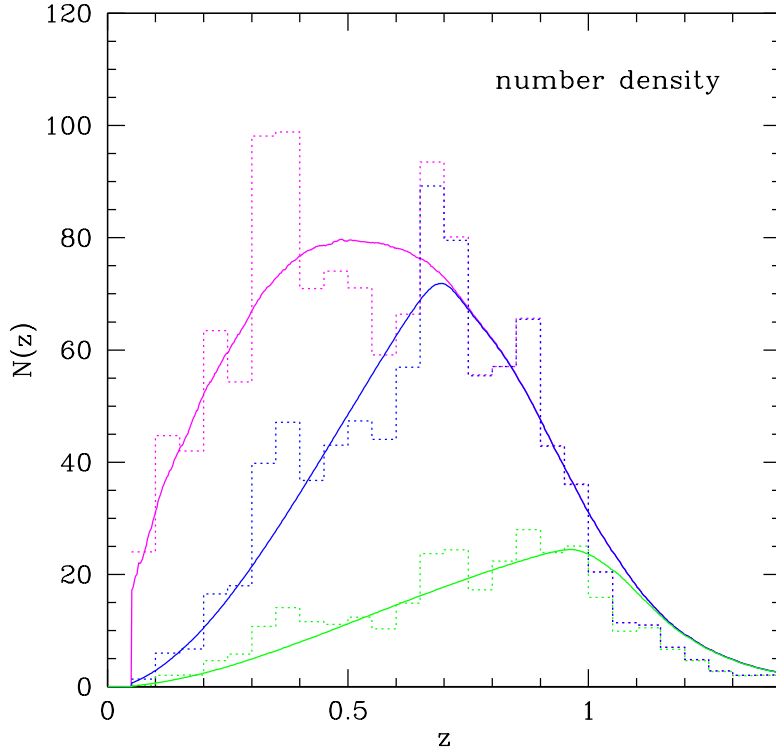


FIG. 2.— Redshift distribution of galaxies in the zCOSMOS area. The continuous lines correspond to the smoothed  $N(z)$  distributions obtained by weighting galaxies according to their  $\Delta V(z)/V_{max}$  contribution in  $\Delta z = 0.002$  intervals as described in the text. The dotted lines correspond to the histogram distributions of tracer galaxies in the redshift bins of  $\Delta z = 0.05$  and they are divided by 25 to match the redshift bin of the smoothed  $N(z)$ . Magenta represents the flux limited sample of tracer galaxies, blue represents the sample of galaxies with  $M_B < -19.3 - z$  and green represents the sample of tracer galaxies with  $M_B < -20.5 - z$ . The last two samples are volume limited up to  $z < 0.7$  (blue curve) and  $z < 1$  (green curve), respectively.

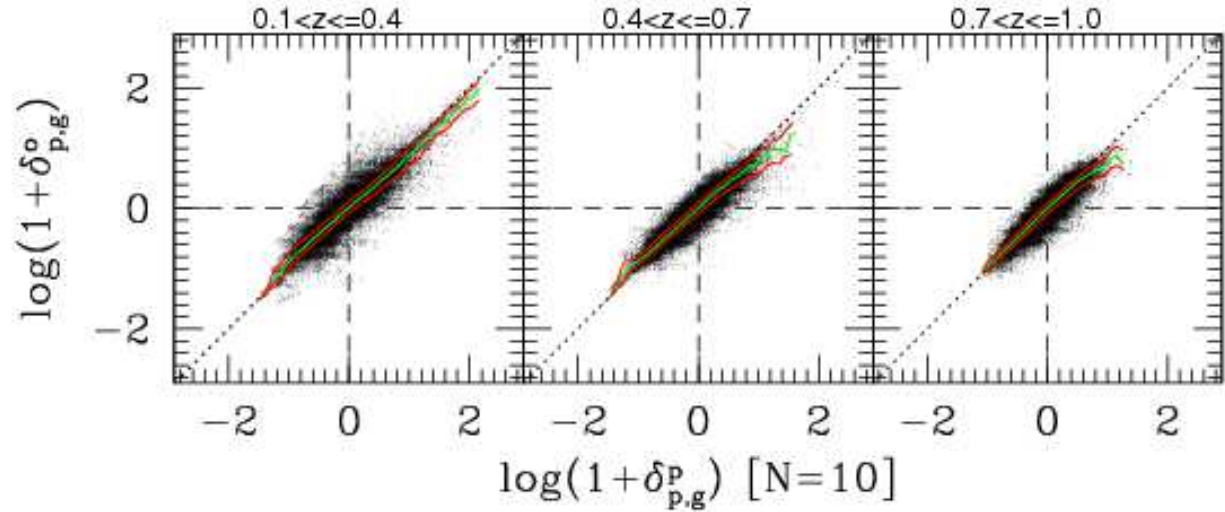


FIG. 3.— Comparison between the 10k+30kZADE observed and 40k parent overdensities. The green line represents the median for the 10kspec+30kZADE observed, the red lines correspond to the 25th and 75th percentiles for the 10kspec+30kZADE observed. Binning is done along the parent overdensity axis. Overdensities are obtained by using the distance to the 10th nearest neighbour. Note that 50% of all points are contained between the red lines. The lower indices  $p$  and  $g$  indicate that the overdensity has been reconstructed using the projected distances to define a smoothing length  $R$  and has been reconstructed on the grid, respectively. The upper index refers to the type of the mock catalogue; “p” stands for the parent and “o” for the observed catalogue. See more details in the text.

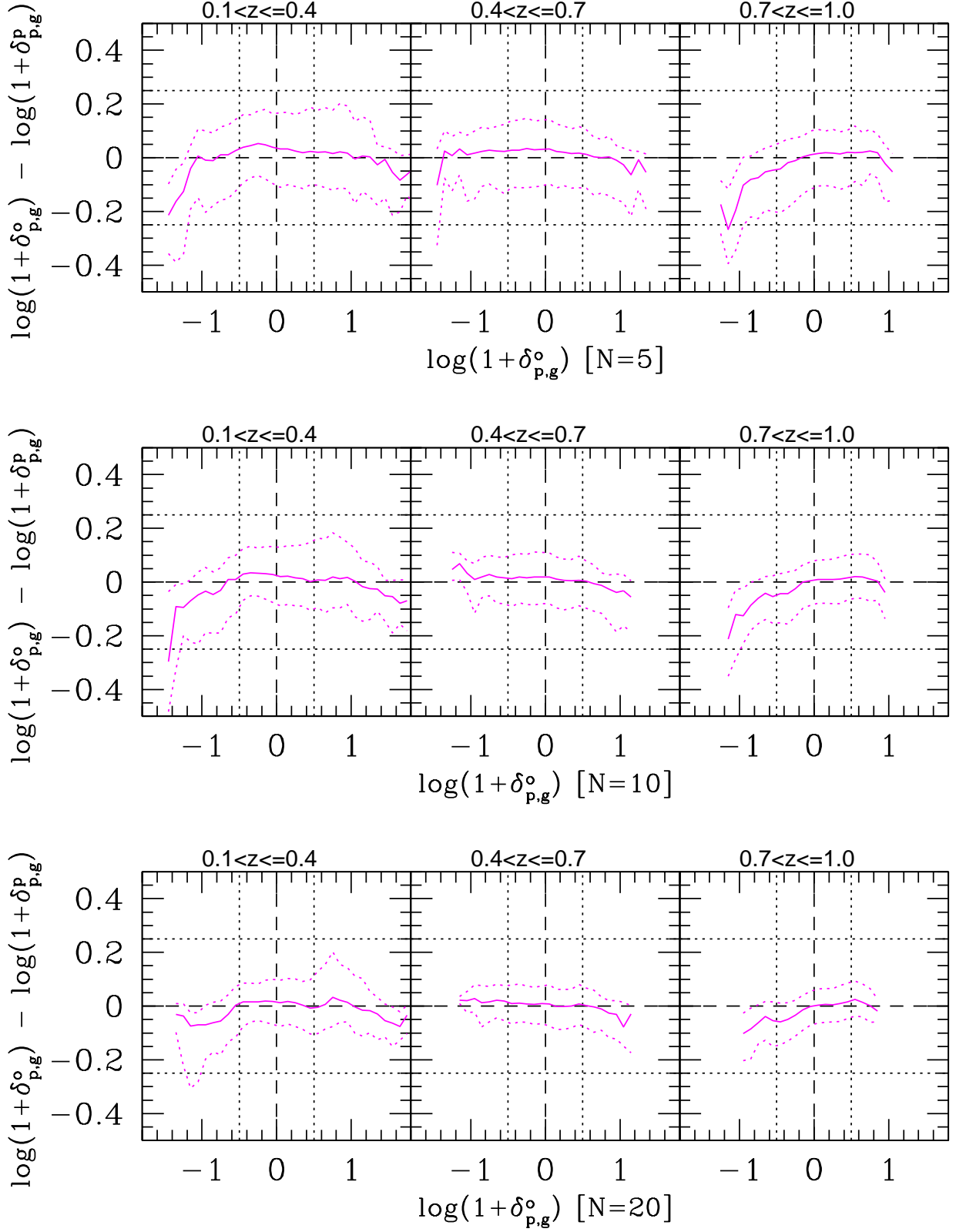


FIG. 4.— The difference between overdensities reconstructed in the observed catalogue, using the ZADE formalism, and in the parent catalogue, plotted as a function of the observed overdensity. The density is obtained by measuring distance to the 5th, 10th and 20th nearest neighbour in the top, middle and bottom panel, respectively. The continuous line represents median for the measured difference between the two reconstructed overdensities, the dotted lines correspond to the 25th and 75th percentiles for this difference. The indices are defined in Figure 3.

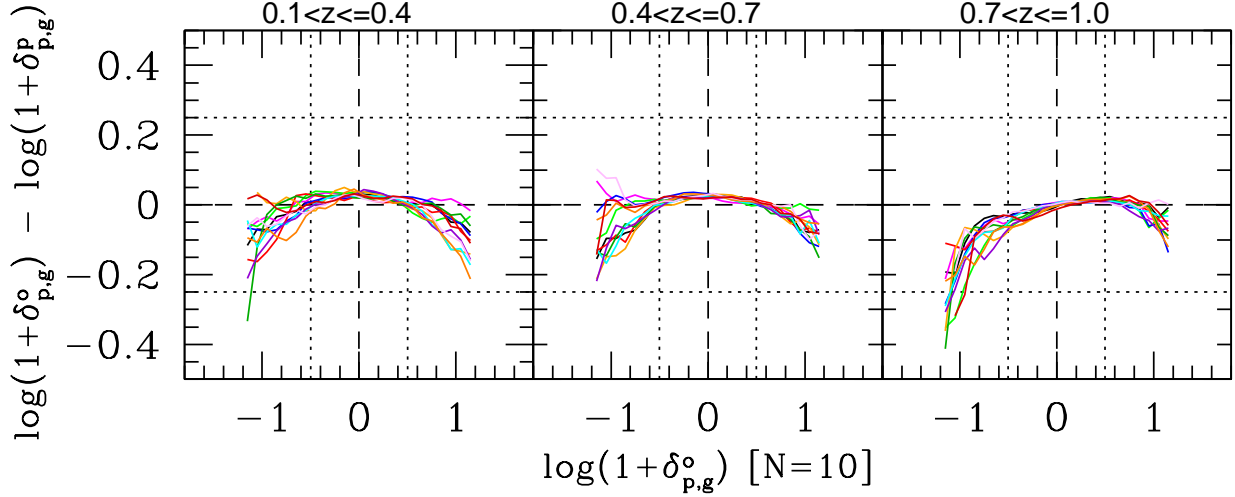


FIG. 5.— The difference between overdensities reconstructed in the observed catalogue, using the ZADE formalism, and parent catalogue, plotted as a function of the observed overdensity. The density is obtained by measuring distance to the 10th nearest neighbour. Each continuous line corresponds to the median of the difference between the two reconstructed overdensities (observed and parent), in the bins of the observed overdensity, for a single mock catalogue. Individual panels include results for 12 mock catalogues. The observed overdensities are presented in the range  $-1.2 < \log(1 + \delta_{p,g}^o) < 1.2$ . The indices are defined in Figure 3.

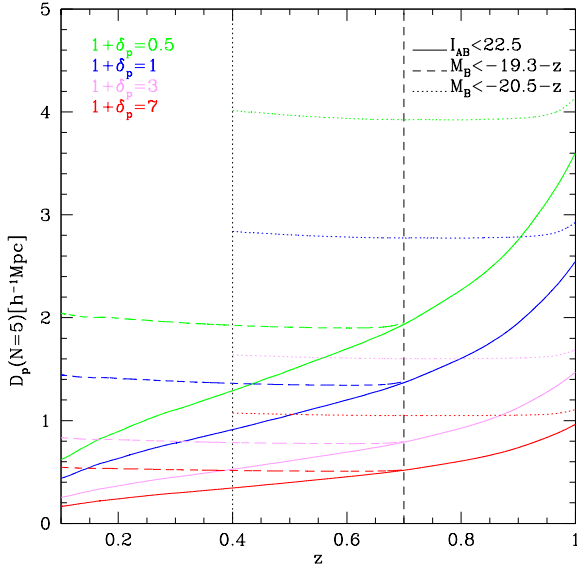


FIG. 6.— Projected distances, defined by the distance to the 5th nearest neighbour, used to define the aperture for the reconstruction of densities centred on the 10k zCOSMOS galaxies. The continuous, long-dashed and short-dashed lines are for the  $I_{AB} < 22.5$ ,  $M_B < -19.3 - z$  and  $M_B < -20.5 - z$  samples of tracer galaxies. The lines for the overdensities of 0.5, 1, 3 and 7 in  $1 + \delta_p$  units are presented in green, blue, pink and red, respectively.

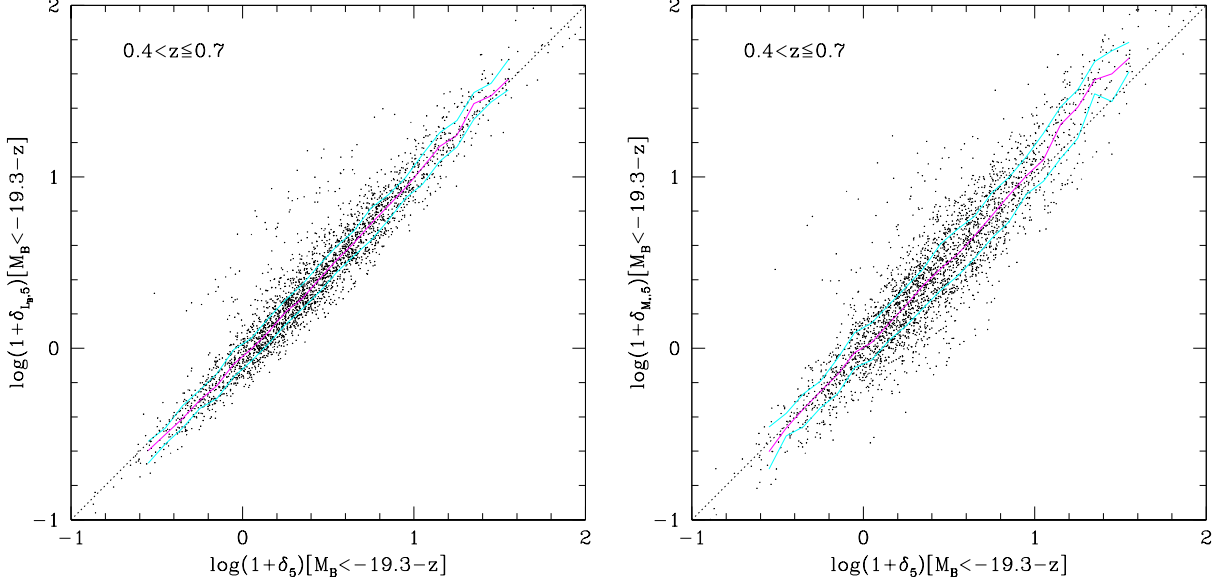


FIG. 7.— Comparison of the overdensities measured around the 10k zCOSMOS galaxies using equation 4 with the  $M_B < -19.3 - z$  volume limited sample of tracer galaxies and within the apertures defined by the distance to the 5th nearest neighbour. We compare the B-band luminosity and stellar mass weighted overdensities to the unity weighted overdensities in the left and right panels, respectively. The magenta line is the median and the cyan lines are the lower and upper quartiles of the presented distributions, where the binning is carried out along the abscissa axis. There is a good correlation between the number overdensities and the  $L_B$  and  $M_*$  weighted overdensities.

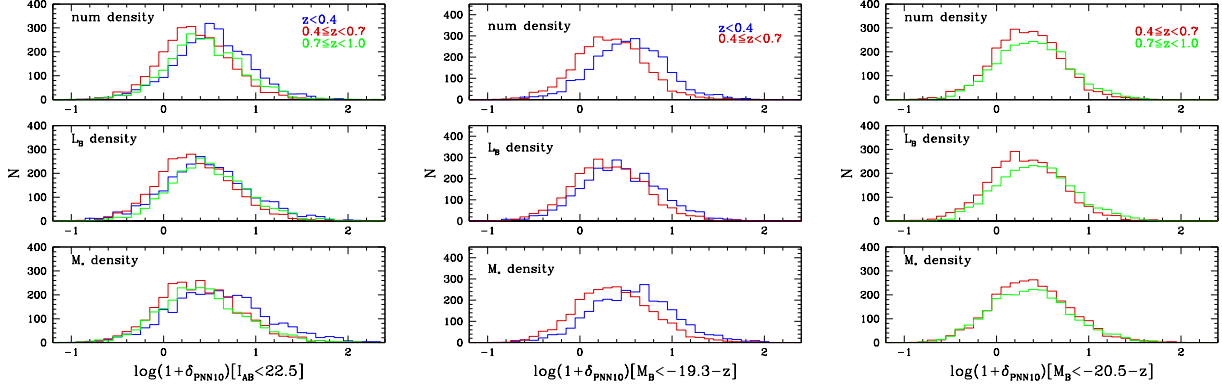


FIG. 8.— Histogram distributions of number of galaxies in the bins of overdensities  $\log(1 + \delta_p)$ . The overdensities are reconstructed at positions of the 10k zCOSMOS galaxies, using the cylindrical adaptive filter  $W$  (equation 4) with smoothing length defined by the 10th nearest neighbour. The distributions are shown separately for three different redshift bins:  $z < 0.4$  (blue),  $0.4 \leq z < 0.7$  (red) and  $0.7 \leq z < 1$  (green). We use mass-weighting  $m_i = 1$ ,  $m_i = L_B$  and  $m_i = M_*$  for the reconstructions presented in the upper, middle and lower panels, respectively. A set of these three distributions of overdensities reconstructed for the  $I_{AB} < 22.5$ ,  $M_B < -19.3 - z$  and  $M_B < -20.5 - z$  samples of tracer galaxies is presented in the left, middle and right, respectively.

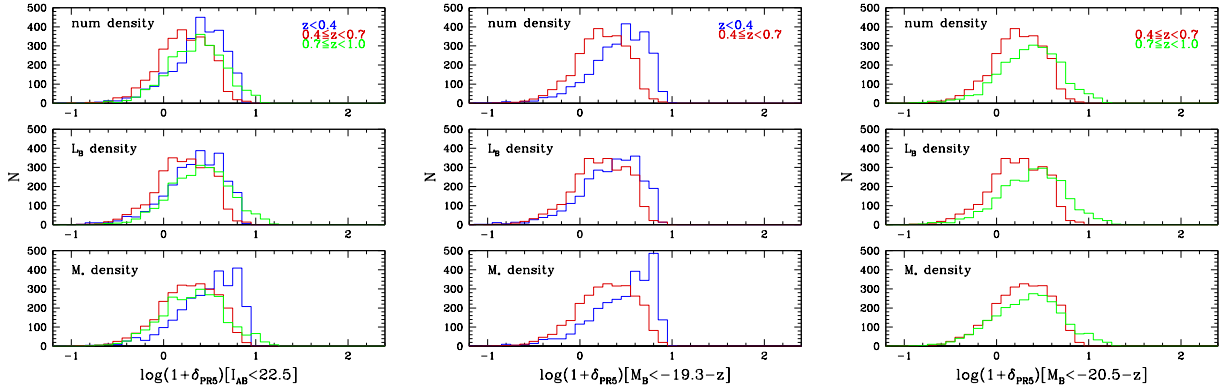


FIG. 9.— Histogram distributions of number of galaxies in the bins of overdensities  $\log(1 + \delta_p)$ . The overdensities are reconstructed at positions of the 10k zCOSMOS galaxies, using the cylindrical fixed filter  $W$  (equation 4) with smoothing length defined to be  $5 h^{-1} \text{Mpc}$ . The distributions are shown separately for three different redshift bins:  $z < 0.4$  (blue),  $0.4 \leq z < 0.7$  (red) and  $0.7 \leq z < 1$  (green). We use mass-weighting  $m_i = 1$ ,  $m_i = L_B$  and  $m_i = M_*$  for the reconstructions presented in the upper, middle and lower panels, respectively. A set of these three distributions of overdensities reconstructed for the  $I_{AB} < 22.5$ ,  $M_B < -19.3 - z$  and  $M_B < -20.5 - z$  samples of tracer galaxies is presented in the left, middle and right, respectively.

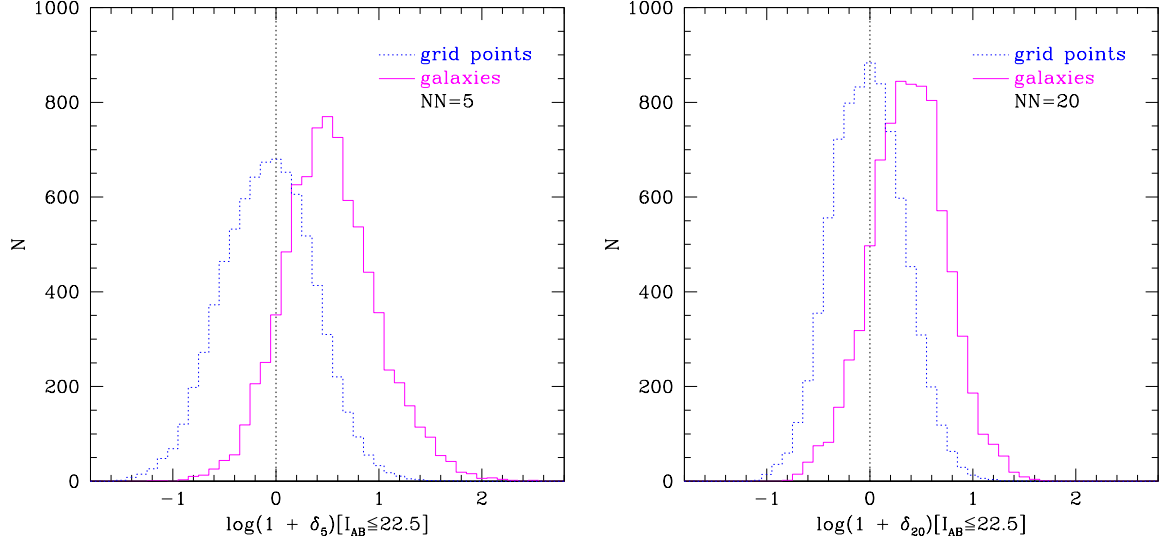


FIG. 10.— Histogram of the overdensities in the zCOSMOS volume calculated on the grid points (blue) and at the positions of zCOSMOS galaxies (magenta). The histogram of the grid points is scaled to the number of galaxies with high quality redshifts. Galaxies are not distributed homogeneously in the zCOSMOS volume, they form clumps of the overdense regions leaving some of the volume empty.

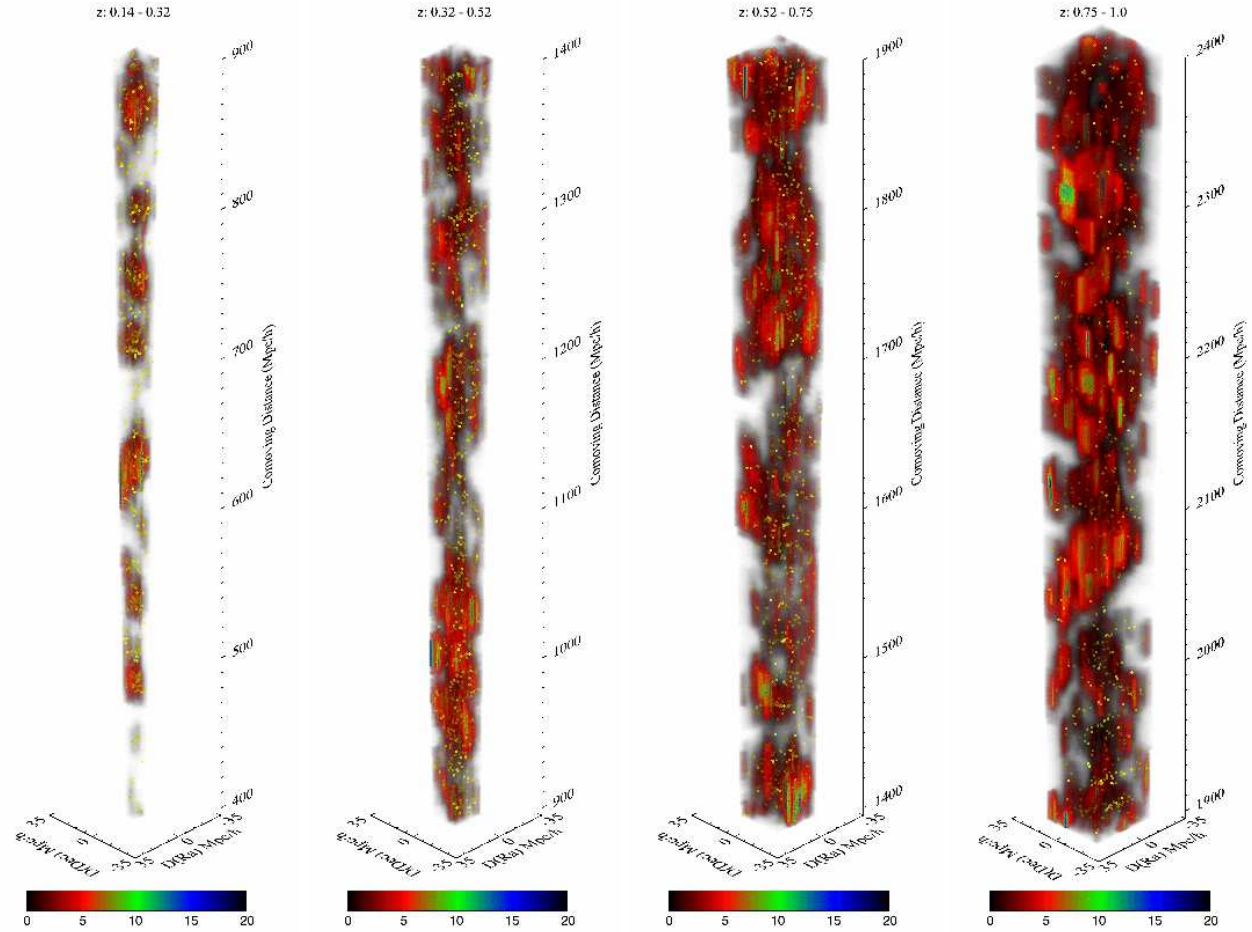


FIG. 11.— Cosmographical tour of the zCOSMOS survey. The 10k zCOSMOS overdensity field is reconstructed on the grid with the flux limited 10kspec+30kZADE sample of tracer galaxies. The aperture is defined by the distance to the 5th nearest neighbour projected within  $\pm 1000 \text{ km s}^{-1}$  to redshift of the individual grid points. All three axis, distance from the survey centre in right ascension, distance from the survey centre in declination and distance (corresponding to redshift), are expressed in comoving  $h^{-1}\text{Mpc}$ . The reconstructed overdensity field yields structures in a large range of comoving scales covering a spectrum of different overdensities at all redshifts reliably probed by the 10k zCOSMOS survey. The colour scale of the  $1 + \delta_p$  values is presented below each cone covering  $500 h^{-1}\text{Mpc}$ . The positions of galaxies are marked with yellow dots.



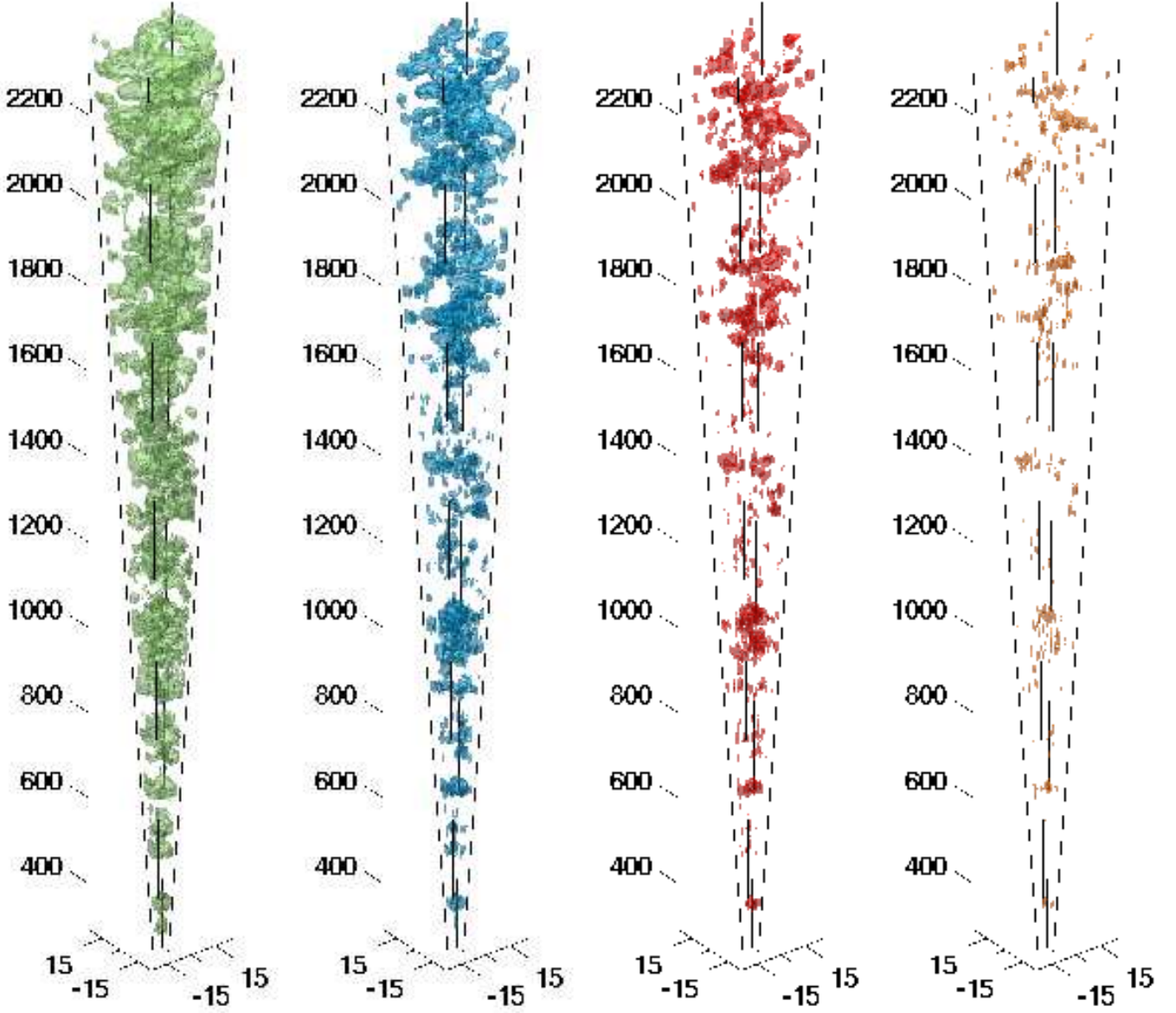


FIG. 12.— Distribution of the overdense structures in the 10k zCOSMOS overdensity field. The structures are defined as isosurfaces enclosing regions with  $1 + \delta_p \geq 1.5, 3, 5$  and  $10$  ( $1 + \delta \geq 1.8, 5.2, 11.2$  and  $31.6$ ) from the left to the right, respectively. Comoving distances in the radial direction correspond to  $0.1 < z < 1$ . The distribution of overdense structures matches the richness and complexity of the local cosmic web up to  $z \sim 1$ . The structures are delineated from the overdensity field reconstructed following the same scheme as in Figure 11. All three axis, distance from the survey centre in right ascension (left hand side axis), distance from the survey centre in declination (right hand side axis) and distance (corresponding to some redshift; vertical axis) are expressed in comoving  $h^{-1}\text{Mpc}$ . The figures are compressed by a factor of  $\sim 3.5$  in redshift direction.

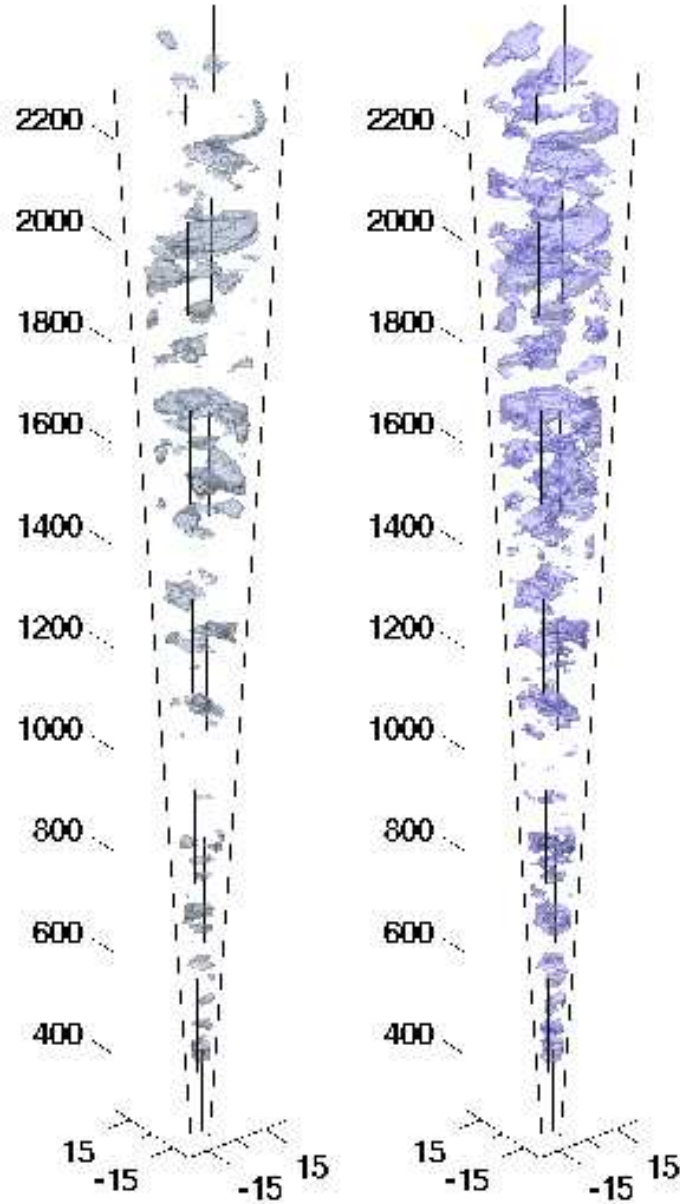


FIG. 13.— The 10k zCOSMOS underdense regions (voids). The structures are defined as isosurfaces enclosing regions with  $1 + \delta_p \leq 0.15$  (6.67 times smaller than  $\bar{\rho}(z)$ ) and 0.25 (4 times smaller than  $\bar{\rho}(z)$ ) in the left and the right cone, respectively. Comoving distances in the radial direction correspond to  $0.1 < z < 1$ . The structures are delineated from the overdensity field reconstructed following the same scheme as in Figure 11. All three axis, distance from the survey centre in right ascension (left hand side axis), distance from the survey centre in declination (right hand side axis) and distance (corresponding to some redshift; vertical axis) are expressed in comoving  $h^{-1}$ Mpc. The figures are compressed by a factor of  $\sim 3.5$  in redshift direction.

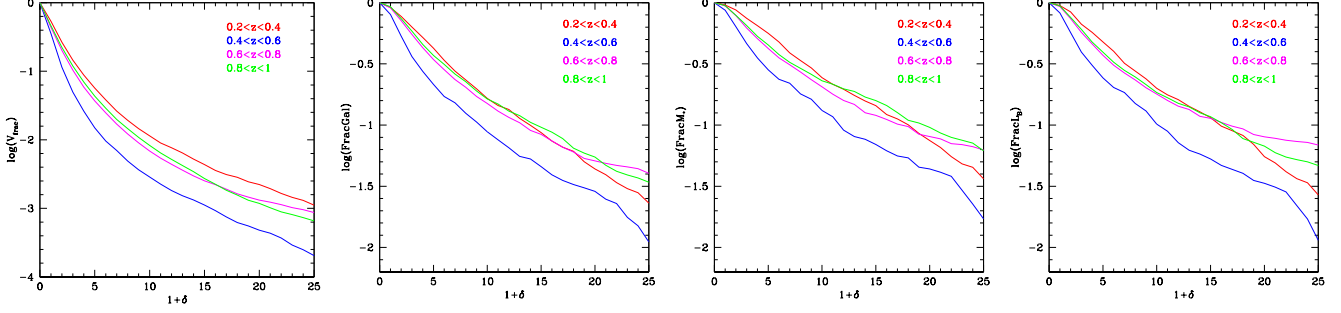


FIG. 14.— Fractions of volume, galaxies, stellar masses and B-band luminosities enclosed in the structures defined by the given overdensity  $1 + \delta_p$  values, going from the left to the right. These fractions are presented in a narrow redshift slices  $\Delta z = 0.2$ , starting from  $z = 0.2$ . The resulting fraction are dominated by cosmic variance. However, it is clear that the overdense structures are much more important in terms of their baryonic content than in the terms of the volume which they occupy. Note the different scale of the y-axis in the first panel.

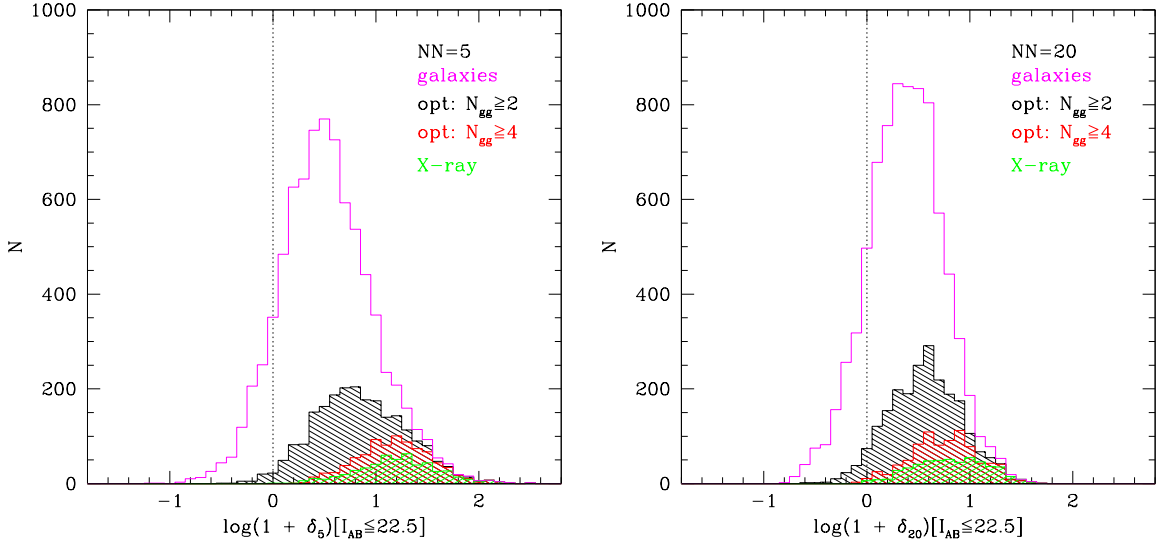


FIG. 15.— Comparison of the overdensities reconstructed at the positions of all zCOSMOS galaxies and those galaxies residing in the virialised structures. The histogram of the overdensities at the positions of zCOSMOS galaxies is presented in magenta. The shaded histograms represent the distribution of overdensities centred on galaxies which reside in the virialised structures: X-ray clusters (green shaded histogram), the optical groups with at least 2 detected members (black shaded histogram) and the optical groups with at least 4 detected members (red shaded histogram). The histograms overlap each other.

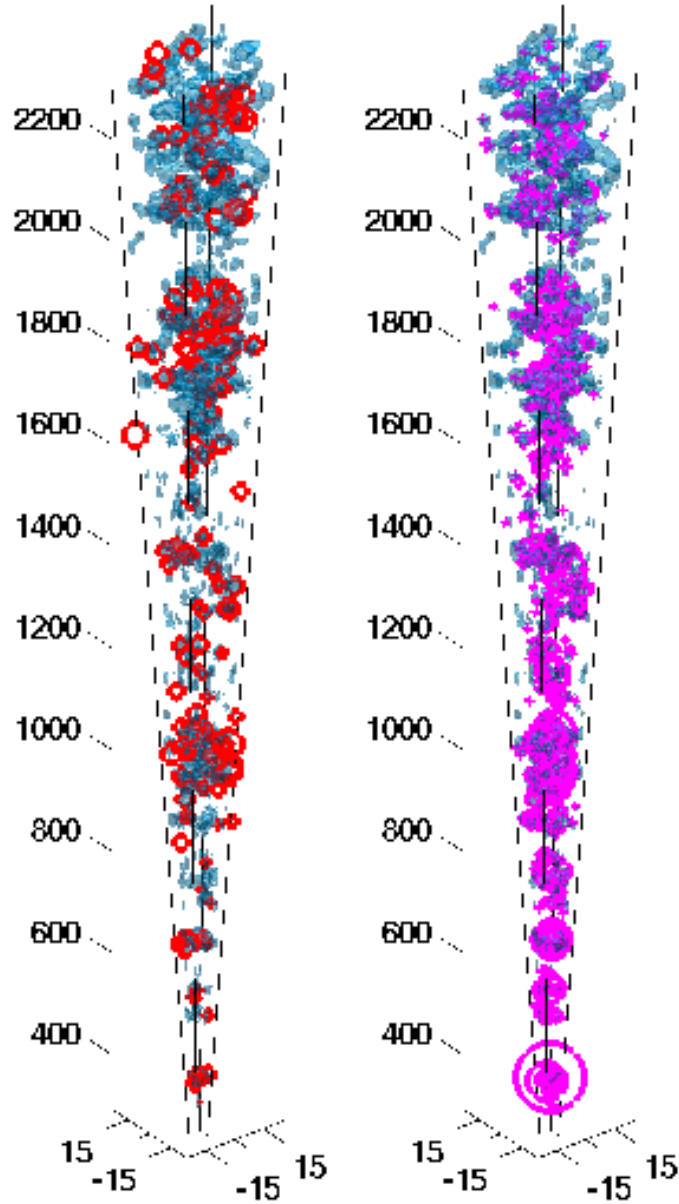


FIG. 16.— Comparison of the zCOSMOS density field to the estimates of the bound structures. On the left and right figures is presented the zCOSMOS density field at  $1 + \delta_p \geq 3$  obtained with the 10k+30kZADE flux limited sample and the apertures defined by the distance to the 10th nearest neighbour projected within  $\pm 1000 \text{ km s}^{-1}$ . On top of the overdensity field are overlaid X-ray detected clusters (red circles, on the left) and optical groups with at least three detected members (magenta circles, on the right). Each circle is centred at the position of the defined structures. Radii of the circles are scaled in  $RA - DEC$  plane to the X-ray luminosity for the X-ray clusters and to the number of detected objects in the optical groups.

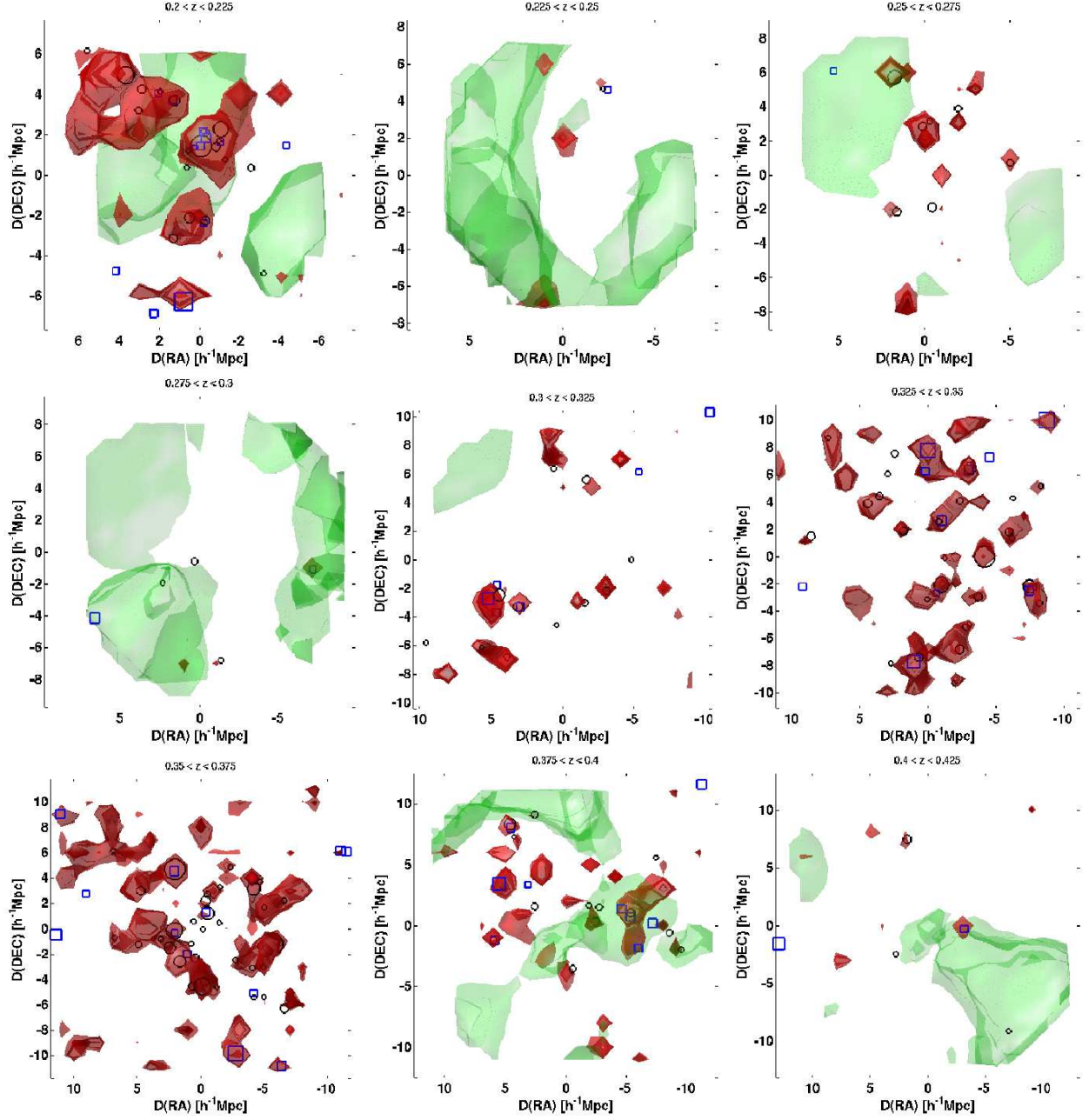


FIG. 17.— The overdensity field of galaxies projected in redshift slices of 0.025 width, covering the redshift interval from 0.2 to 1. The overdensity field is reconstructed using the flux limited sample of galaxies within the apertures defined by the 5th nearest neighbour projected within  $\pm 1000 \text{ km s}^{-1}$ . Only structures defined by the isosurface contours of  $1 + \delta_p \geq 6.67$  (red) and  $1 + \delta_p \leq 0.15$  (green) are shown. As a comparison, the optical groups in the same redshift bins with at least 3 detected members are overplotted as circles and X-rays clusters as squares. The sizes of the symbols to mark the positions of the virialised structures are scaled as in Figure 16. The redshift slices 0.3 – 0.375, 0.675 – 0.75 and 0.875 – 1 are dominated by the overdense structures. Large,  $RA - DEC$ -extended underdense structures are detected in the 0.45 – 0.5, 0.525 – 0.55, 0.575 – 0.6, 0.625 – 0.675 and 0.8 – 0.825 redshift slices.

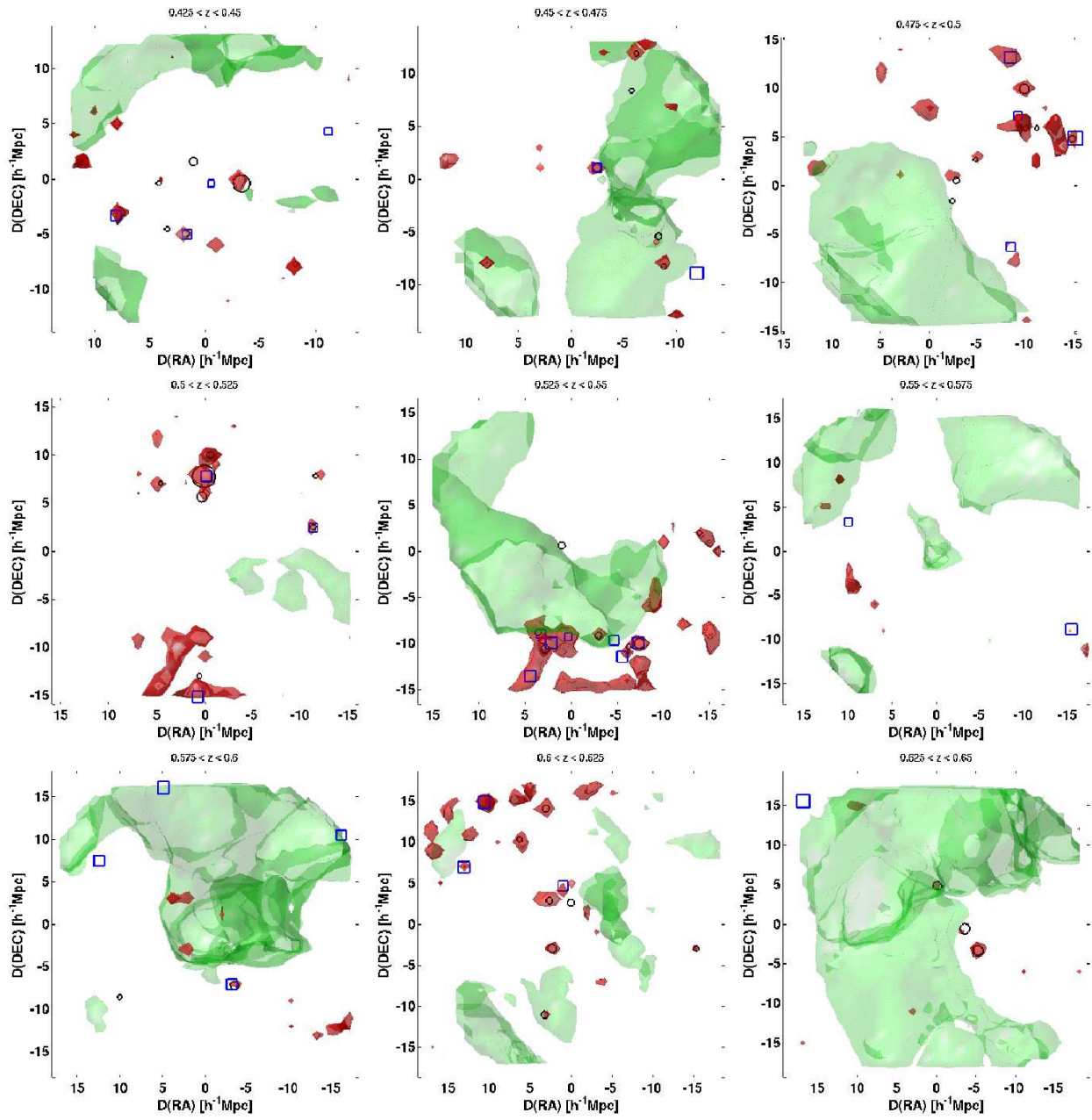


FIG. 17.— Continued.



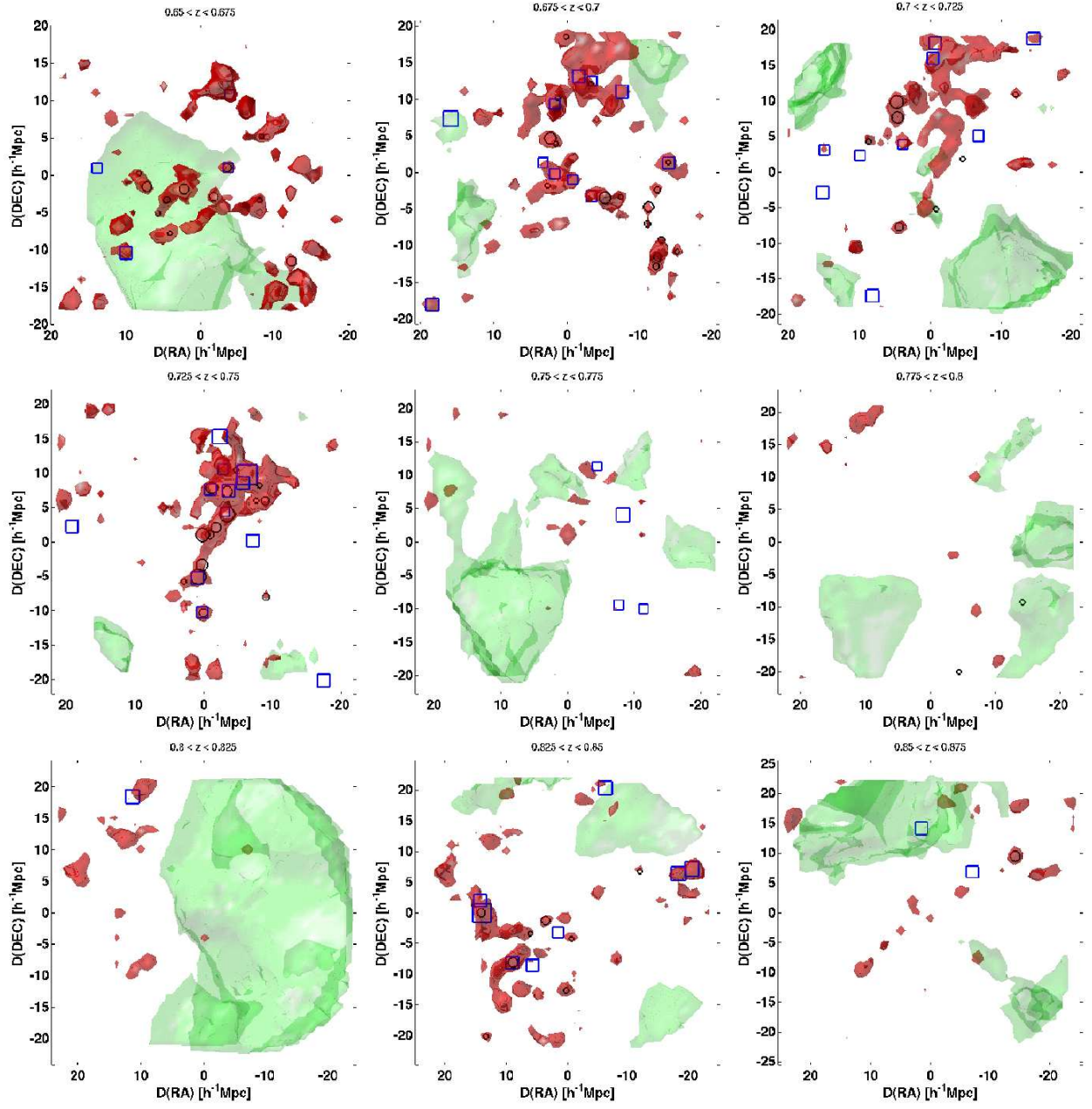


FIG. 17.— Continued.

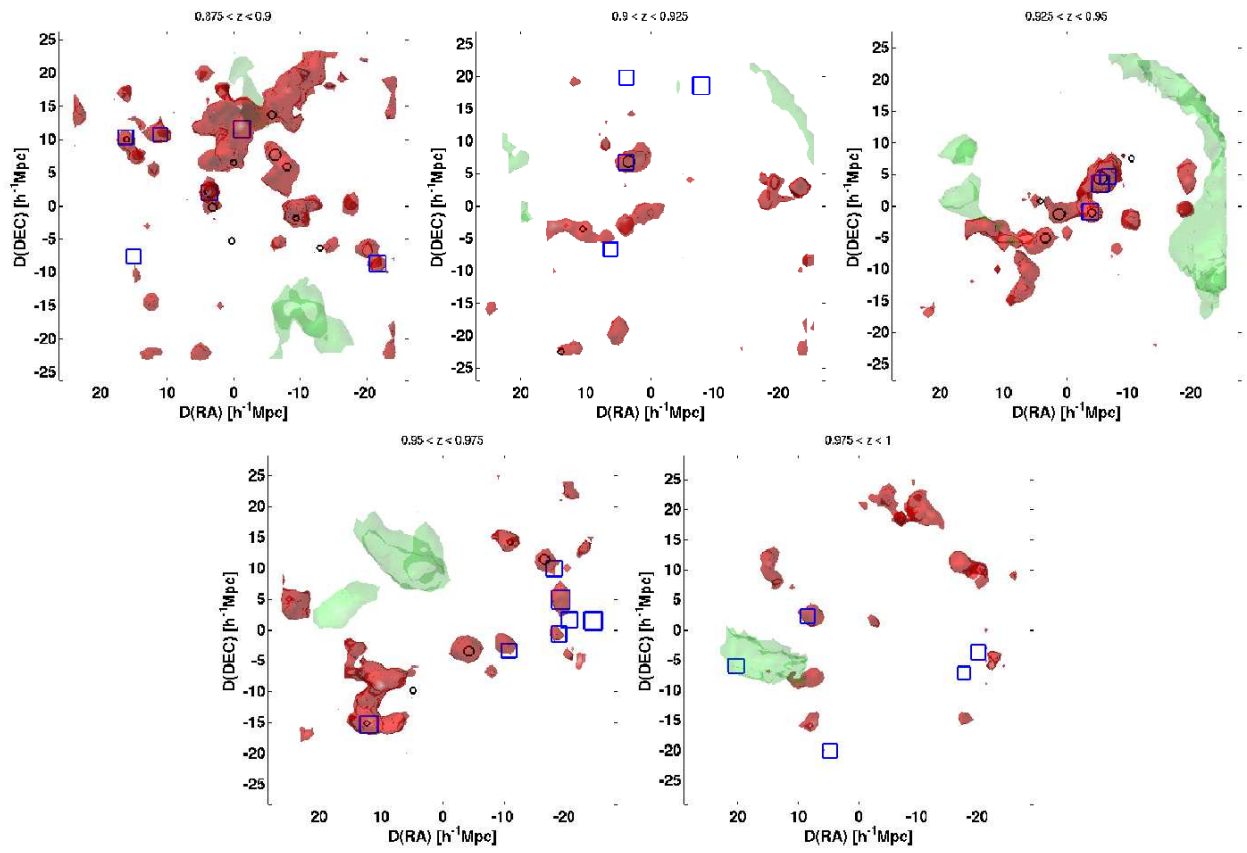


FIG. 17.— Continued.



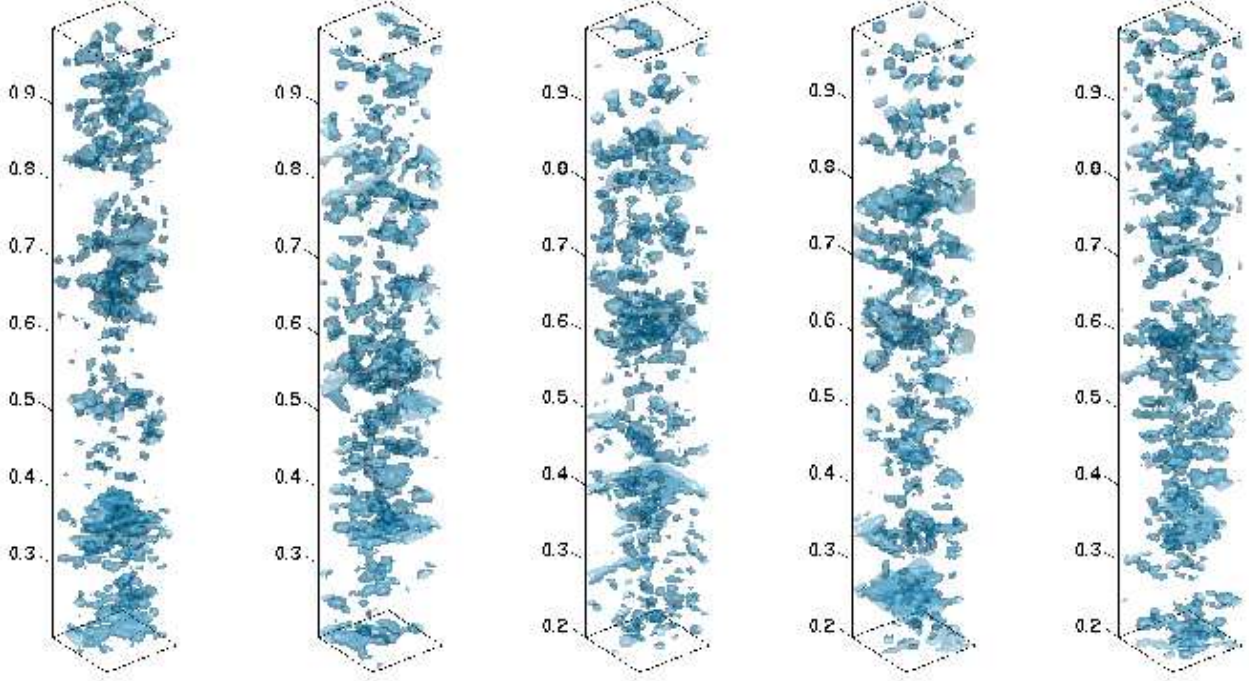


FIG. 18.— Comparison of the  $1 + \delta_p = 3$  isosurfaces in the overdensity field reconstructed using the 10k zCOSMOS sample of flux limited tracer galaxies and the equivalent sample of galaxies in the mock catalogues. First left hand figure: overdensity field reconstructed using the real 10k+30kZADE zCOSMOS galaxies. Rest of figures: overdensity field reconstructed using the mock 10k+30kZADE samples. In every point the overdensity field is reconstructed by counting the number of objects with an integrated ZADE-modified probability distribution in the apertures defined by the distance to the 10th nearest neighbour projected within  $\pm 1000 \text{ km s}^{-1}$  of the redshift of the grid point. The grid is regular in  $\Delta RA = \Delta DEC = 2 \text{ arcmin}$  and  $\Delta z = 0.002$ . The overdensity values are presented without the edge correction. The high complexity of the cosmic web is noticeable in all figures. It appears that there are more structures on large scales ( $\sim 10 \text{ h}^{-1} \text{ Mpc}$ ), visible above  $z \sim 0.8$ , in the real data than in the mock catalogues. To highlight the structures in the figures, we omit the axis. The transversal axis are RA and DEC, covering the zCOSMOS area  $\sim 1 \text{ deg}^2$ , and the vertical axis is redshift in the range  $0.2 < z < 1$ .

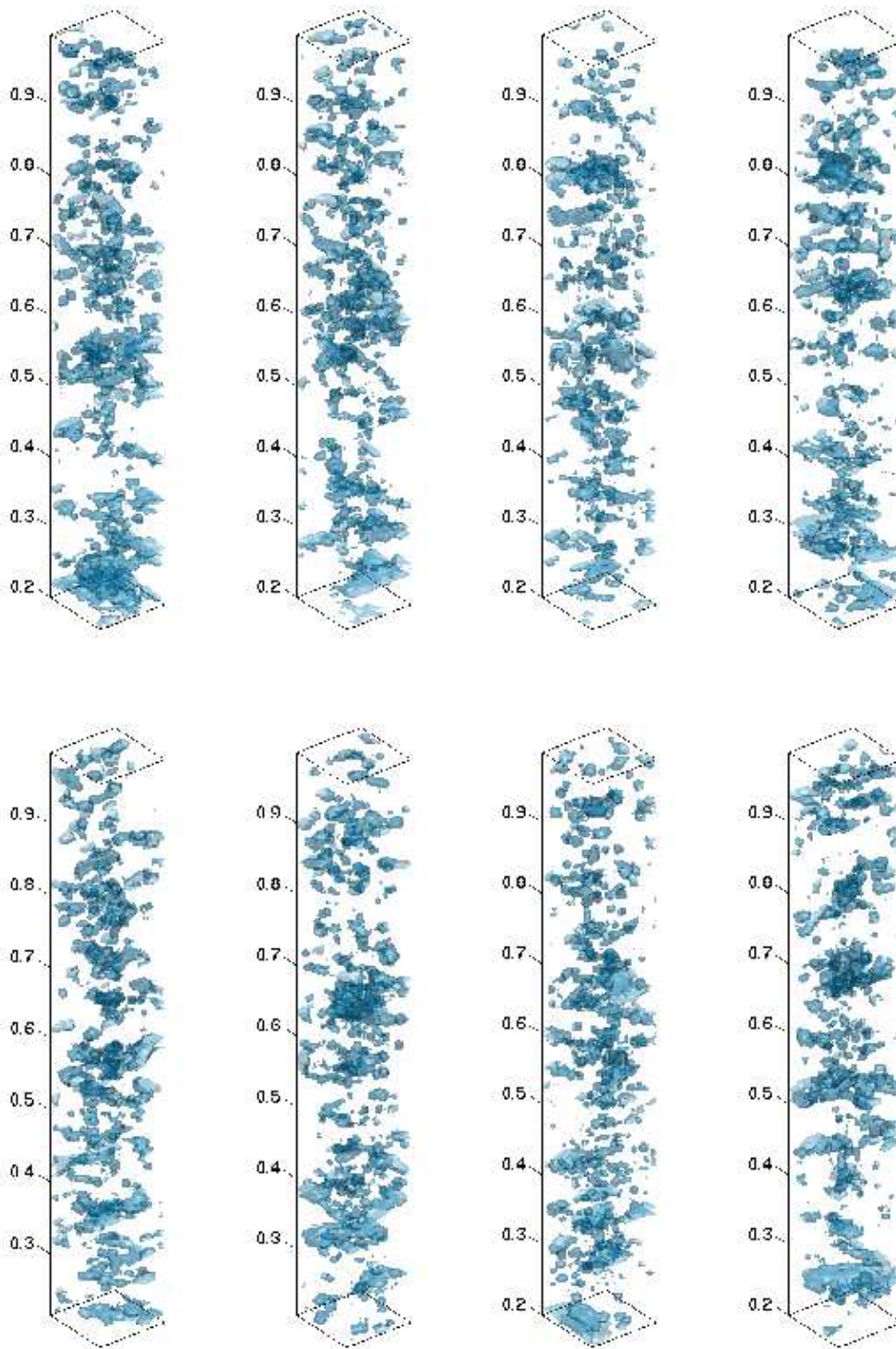


FIG. 18.— Continued.

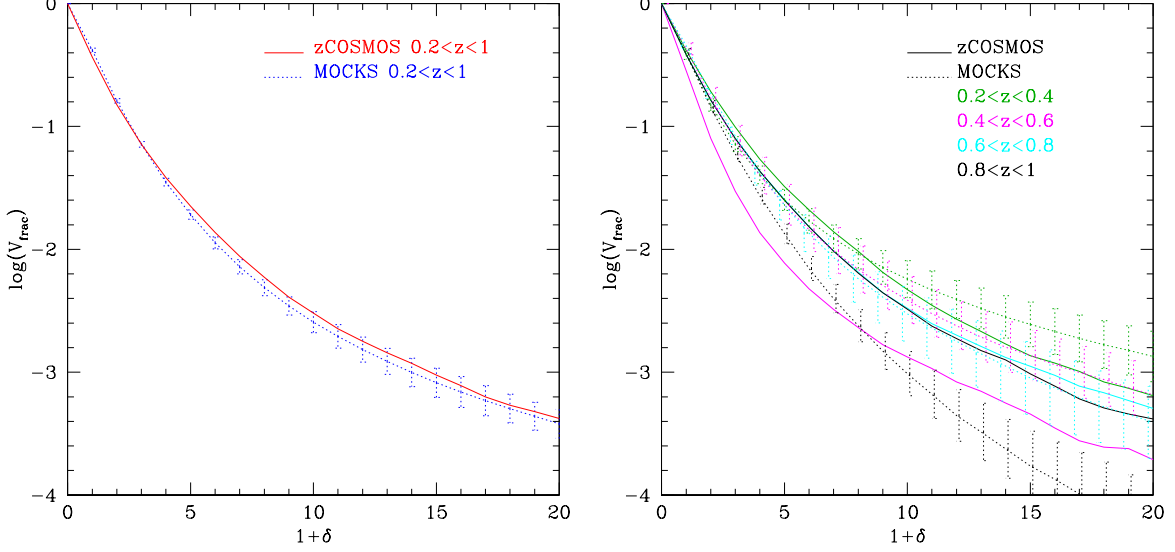


FIG. 19.— Fraction of the volume with the overdensity  $\delta_p$  above a given value. The aperture in the overdensity field is defined using the distance to the 10th nearest neighbour projected to the redshift of the grid point within  $\pm 1000 \text{ km s}^{-1}$ . A mock value is obtained by averaging results obtained from the individual 12 mock catalogues. The error is calculated as the standard deviations from the individual mock catalogue results. The continuous lines are for the real data, the dotted lines are for the corresponding mock catalogues. Volumes are estimated in  $[\text{h}^{-1}\text{Mpc}]^3$ . Left: Statistics in  $0.2 < z < 1$ . The dashed red lines are for the real data, the continuous blue lines are the corresponding mock catalogues. Right: Statistics in four redshift bins:  $0.2 < z < 0.4$  (green),  $0.4 < z < 0.6$  (magenta),  $0.6 < z < 0.8$  (cyan) and  $0.8 < z < 1$  (black).

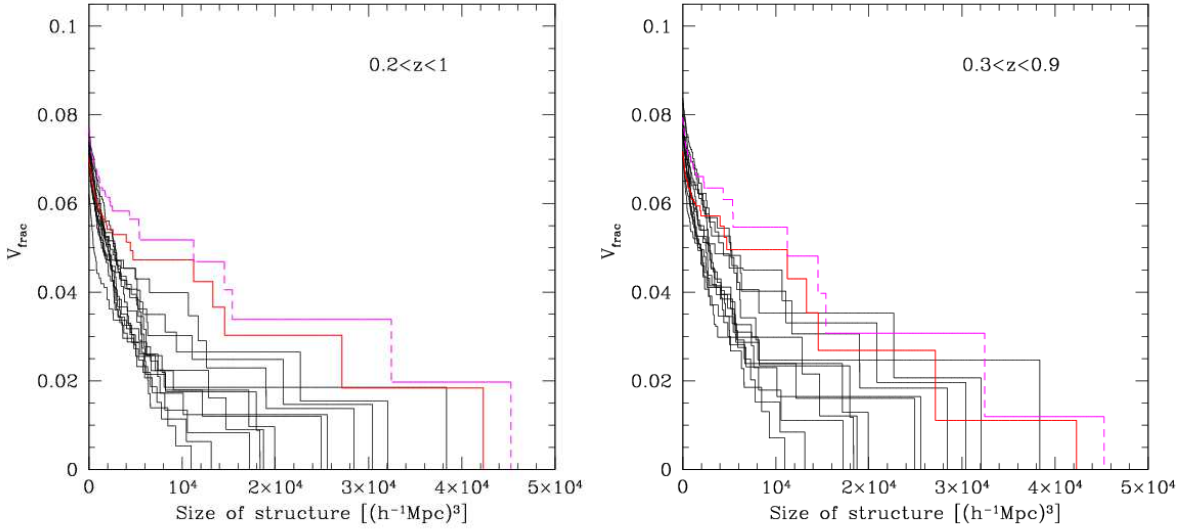


FIG. 20.— A comparison of the sizes of the structures above  $1 + \delta_p \geq 3$  in the data [red:  $V/V_{max}$  smoothing to obtain  $N(z)$ , magenta: smoothing equivalent to the smoothing applied to the mock  $N(z)$ ] and in the individual mock catalogues (black curves). The curves correspond to the volume fractions contained within the structures of at least the size indicated on the x-axis, where size is measured in  $[\text{h}^{-1}\text{Mpc}]^3$ . There is not a single mock catalogue which contains as much volume as the real data in the large structures in  $0.2 < z < 1$ . When we limit our statistics to  $0.3 < z < 0.9$ , the data results falls within the statistics outlined by the mocks. Difference between the data and the mocks at the large sizes is dominated by the structure at  $z \sim 0.9$ .